mTOR inhibition in Q175 Huntington's disease model mice facilitates neuronal autophagy and mutant huntingtin clearance

Philip Stavrides[1], Chris N. Goulbourne[1], James Peddy[1], Chunfeng Huo[1], Mala Rao[1, 2], Vinod Khetarpal[5], Deanna M. Marchionini[5], Ralph A. Nixon[1, 2, 3, 4, #], Dun-Sheng Yang[1, 2, @]

[1]Center for Dementia Research, Nathan S. Kline Institute, Orangeburg, NY 10962 USA; Departments of [2]Psychiatry and [3]Cell Biology, and [4]NYU Neuroscience Institute, New York University Grossman School of Medicine, New York, NY 10016 USA; [5]CHDI Management/CHDI Foundation, New York, NY 10001 USA.

[@] Correspondence: Dun-Sheng.Yang@NKI.RFMH.ORG

[#] **Lead contact:**

Ralph A. Nixon, MD, PhD

Center for Dementia Research

Nathan S. Kline Institute

140 Old Orangeburg Road

Orangeburg, NY 10962

Phone: (845) 398-5423

Fax: (845) 398-5422

Email: Ralph.Nixon@NKI.RFMH.ORG

ABSTRACT

Huntington's disease (HD) is caused by expansion of the polyglutamine stretch in huntingtin protein (HTT) resulting in hallmark aggresomes/inclusion bodies (IBs) composed of mutant huntingtin protein (mHTT) and its fragments. Stimulating autophagy to enhance mHTT clearance is considered a potential therapeutic strategy for HD. Our recent evaluation of the autophagic-lysosomal pathway (ALP) in human HD brain reveals upregulated lysosomal biogenesis and relatively normal autophagy flux in early Vonsattel grade brains, but impaired autolysosome clearance in late grade brains, suggesting that autophagy stimulation could have therapeutic benefits as an earlier clinical intervention. Here, we tested this hypothesis by crossing the Q175 HD knock-in model with our autophagy reporter mouse TRGL (**T**hy-1-**R**FP-**G**FP-**L**C3) to investigate *in vivo* neuronal ALP dynamics. In the Q175 and/or TRGL/Q175 mice, mHTT was detected in autophagic vacuoles and also exhibited high level colocalization with autophagy receptors p62/SQSTM1 and ubiquitin in the IBs. Compared to the robust lysosomal pathology in late-stage human HD striatum, ALP alterations in Q175 models are also late-onset but milder that included a lowered phospho-p70S6K level, lysosome depletion and autolysosome elevation including more poorly acidified autolysosomes and larger-sized lipofuscin granules, reflecting impaired autophagic flux. Administration of a mTOR inhibitor to 6-mo-old TRGL/Q175 normalized lysosome number, ameliorated aggresome pathology while reducing mHTT-, p62- and ubiquitin-immunoreactivities, suggesting beneficial potential of autophagy modulation at early stages of disease progression.

INTRODUCTION

Huntington's disease (HD) is an autosomal dominant disorder caused by a mutation in the gene encoding the huntingtin protein (HTT) resulting in expansion of the polyglutamine (polyQ) stretch on its amino-terminus (The-Huntington's-Disease-Collaborative-Research-Group 1993, Bates, Dorsey et al. 2015, Jiang, Handley et al. 2023, Franklin, Teive et al. 2024). HD pathogenesis advances in a spatiotemporal pattern, which is used to stage disease pathology severity as Grade 0-4 (HD0, HD1, HD2, etc.)(Vonsattel, Myers et al. 1985). GABA-containing medium spiny projection neurons in the striatum are most susceptible to cell death (Vonsattel 2008), and the cerebral cortex, particularly layer 5a, also shows cell loss (Sotrel, Paskevich et al. 1991, Pressl, Mätlik et al. 2024). Neuronal intranuclear inclusions (NIIs) and neuropil inclusions are present in HD brains and are positive for mutant huntingtin (mHTT) and ubiquitin (Ub) (DiFiglia, Sapp et al. 1997, Gutekunst, Li et al. 1999).

Recently, we completed a comprehensive evaluation of the autophagic-lysosomal pathway (ALP) in the HD brain at progressive disease stages, focusing on the most affected brain region, the striatum, in comparison to a less affected region, the neocortex (Berg, Veeranna et al. 2024 bioRxiv). Double fluorescence immunolabeling and immuno-electron microscopy (IEM) revealed colocalization of HTT/mHTT with the autophagy-related adaptor proteins, p62/SQSTM1 and ubiquitin, and cathepsin D (CTSD) within aggresome inclusions and autophagic compartments, documenting the involvement of ALP in HTT/mHTT turnover and the disease-related impairment of this process in late-stage disease. The temporal evolution of ALP alterations generally revealed minimal detectable impairment of upstream autophagy steps [e.g., autophagosome (AP) induction, formation, and fusion with lysosomes (LY)] and, in striatum, elevated levels of LAMP1 and LAMP2 markers suggesting modestly upregulated LY biogenesis. At late disease stages, mainly HD4, neuronal ALP dysfunction exhibited enlarged/clumped CTSD-immunoreactive autolysosomes (AL)/LY and ultrastructural evidence of autophagic vacuole (AV) fusion and transition to lipofuscin granule formation. These findings collectively suggest that a relatively competent autophagy machinery is maintained during the disease progression with a compensatory upregulation in lysosomal biogenesis, which together prevents against mHTT accumulation. This situation is failing at the late disease stages when AL clearance is impeded, substrates, including mHTT and its metabolites, accumulate in AL and aggresome inclusions increase.

A possible implication of the foregoing findings is that pharmacologic enhancement of autophagy applied at a symptomatic but early stage of disease, when the ALP clearance machinery is fully competent, may be therapeutic in clearing mHTT protein in affected neurons. By contrast, in Alzheimer's Disease (AD) lysosomal clearance deficits develop at the earliest disease stages, suggesting enhanced autophagy induction is counterproductive.

Modulation of autophagy as a therapeutic strategy for HD has been investigated in various cell and animal models of HD (Sarkar and Rubinsztein 2008, Boland, Yu et al. 2018, Kim, Lalonde et al. 2021, Jiang, Handley et al. 2023, Yang and Zhang 2023). Of particular relevance to our present study are those involving autophagy induction with mTOR-dependent or -independent autophagy-enhancing approaches in HD mouse models [e.g. Trehalose (Tanaka, Machida et al. 2004); Rapamycin analog Temsirolimus (CCI-779) (Ravikumar, Vacher et al. 2004); Rilmenidine (Rose, Menzies et al. 2010); Rhes manipulations (Baiamonte, Lee et al. 2013, Lee, Tecedor et al. 2015)]. These studies have generally demonstrated ameliorative effects on outcome measures such as mHTT lowering and behavioral/motor function assays. However, in many cases it is unclear whether autophagy mechanisms are directly engaged in the brain or are critical to rescue.

Thus, our study aimed to comprehensively characterize the autophagy response with a range of autophagy markers to interrogate the competence of the entire autophagy process in relationship to mHTT in the well-characterized zQ175 Knock-In HD mouse model (Q175). Towards this goal, we evaluated autophagy in neurons of Q175 after introducing by neuron-specific transgenesis the dual fluorescence-tagged autophagy probe, **t**andem **f**luorescent mRFP-eGFP-**LC3** (tfLC3), an autophagy adaptor protein associated with AP and metabolized via autophagy (Lee, Rao et al. 2019). We thereby generated a new Q175 cross, namely TRGL **(T**hy-1-**R**FP-**G**FP-**L**C3)/Q175. tfLC3 expression, driven postnatally by the neuron-specific Thy1-promoter, allows for selective monitoring of neuronal autophagy without the confounding influence of glial cells. Resolution and sensitivity in reporting tfLC3 signal is high compared to conventional immunofluorescence staining of LC3. The ability to ratiometrically report pH-dependent changes in fluorescence wavelength (hue angle) enables neutral pH AP to be distinguished from acidic AL, that progressively acidify intraluminally upon fusion with LY. We are further able to differentiate AL subgroups differing in their extent of acidification after LY fusion. Distinguishing properly acidified AL from those poorly acidified because of delayed or defective acidification is assisted by immunolabeling AL with a marker, such as cathepsin D, which is then detected with a third

106 fluorophore. Together this triple fluorescence paradigm objectively quantified by computer-
107 assisted deconvolution of the proportions of each label within the analyzed neuron, a reflection of
108 their relative pH (and fusion with LY), which allows ALP organelle subtypes including LC3-
109 nagative LY to be identified and quantified for their numbers, sizes and spatial distributions in
110 intact brain sections. The collective data provides reports on the completion (or lack thereof) of
111 autophagy flux (ALP dynamics) and any blockage at particular steps in the ALP pathway,
112 including the normal acidification and further maturation of AL through their successful
113 elimination of fluorescence-tagged LC3 (Lee, Rao et al. 2019, Lie, Yang et al. 2021, Lee, Yang et
114 al. 2022, Lie, Yoo et al. 2022).

115 Crossing TRGL mice with a model of a neurodegenerative disease, the Q175 mouse model of
116 HD, has enabled us to assess disease-related autophagy alterations in the Q175 and TRGL/Q175
117 models and their response to a pharmacological inhibition of mTOR, (mTORi) INK-128 (hereafter
118 INK). Our data demonstrate target engagement and positive effects of the compound on rescuing
119 Q175 phenotypes including reversal on AL/LY subtypes as reported by the tfLC3 probe and
120 parallel reductions of mHTT-, p62- and Ub-immunoreactivity (IR), suggesting that the compound
121 targeted the ALP to degrade mHTT.

122

123

124 **RESULTS**

125 **Identification of inclusions and HTT molecular species in Q175 mice**

126 Immunohistochemistry (IHC) experiments with the antibody mEM48, which preferentially
127 recognizes aggregated mHTT (Gutekunst, Li et al. 1999), revealed age-dependent development of
128 mHTT-positive profiles in the striatum of Q175KI mice. Brain sections from 2.5-mo-old Q175
129 (not shown) only exhibited faint and diffuse nuclear mHTT staining without identifiable
130 aggresomes/inclusion bodies (IBs), while at 6 and 10 months of age, mHTT-positive IBs were
131 readily detected progressively with age (Fig. 1A2-A3). There were no similar mHTT
132 immunoreactive puncta in WT striatum (Fig. 1A1). These observations are consistent with
133 previous findings in Q175 and other HD mouse models (Li, Li et al. 1999, Menalled, Sison et al.
134 2003, Carty, Berson et al. 2015). To further determine the locations of mHTT IBs in Q175,
135 mEM48-immunostained sections were counterstained with cresyl violet (Fig. 1A4) to distinguish
136 nuclear IBs (Fig. 1A4, arrowheads) from extranuclear IBs, which were localized predominantly in

137 the neuropil (Fig. 1A4, arrows) and also detected rarely in the cytoplasmic portion of the
138 perikaryon. Thus, our results demonstrate age-dependent increase in mHTT aggresomes in the
139 Q175 model.

140 To reveal the ultrastructural locations and features of the mHTT aggregates, immunogold EM
141 (IEM) with antibody mEM48 was performed. EM images (Fig. 1B) demonstrated that the IEM
142 with this antibody was highly specific in detecting mHTT IBs which were localized in the neuronal
143 nuclei, dendrites and axons. Ultrastructurally, most IBs were cotton-ball shaped and composed of
144 fine fibrous or granular elements, somewhat similar to the unbundled short fibrils/protofibrils
145 found *in vitro* with recombinant mHTT protein fragments (Ko, Isas et al. 2018, Kolla, Gopinath et
146 al. 2021, Mario Isas, Pandey et al. 2021), and similar to the structure of NII type inclusions we
147 found in the human HD brain (Berg, Veeranna et al. 2024). Notably, however, human neuritic IBs
148 often displayed a more heterogeneous composition, such as fine fibrils mixed with AVs or bundles
149 composed of microtubule-like filaments, which were not found in the mouse neuritic IBs. Thus,
150 the result suggests a homogenous aggresome pathology in the mouse model, possible reflecting a
151 more rapid formation rate than in human.

152 Previous immunoblotting studies have observed fragmentation of mHTT molecules in the
153 human brain (Kim, Yi et al. 2001, Mende-Mueller, Toneff et al. 2001), including our own study
154 which detects mHTT fragments of 45-48 kDa, which predominantly exist in HD striatum (Berg,
155 Veeranna et al. 2024). To assess HTT molecular species in the Q175 mouse brain, we employed
156 multiple antibodies that preferentially detected mHTT over wild type HTT, including MAB1574
157 (Clone 1C2) (Fig. 1C1, C2), its epitope containing a 38-glns stretch (Trottier, Lutz et al. 1995),
158 and mAb PHP2 (Fig. 1C1), reacting with the peptide sequence QAQPLLPQP within the proline
159 rich domain of HTT (Ko, Isas et al. 2018). Both detected full-length mHTT and a ~120 kDa
160 fragment in the Q175 model (Figs. 1C1; 1C2 left and 1C3 top two graphs). By contrast, MAB5490
161 (Fig. 1C2 right), reacting with aa115-129 of HTT (C-terminal to the region of polyQ stretch-
162 containing exon 1), detected both wild type and mutant forms of HTT (Fig. 1C3, bottom right
163 graph). A ~48 kDa HTT fragment may correspond to the 45-48 kDa fragment seen in human brain
164 (Berg, Veeranna et al. 2024), and was detected by both MAB1574 and MAB5490 antibodies in
165 some samples (Fig. 1C2) but its levels in the Q175 models and the control TRGL were not
166 statistically significantly different (Fig. 1C3, bottom left graph). Thus, the result suggests that HTT

167 fragmentation is not obvious in the Q175 brains, unlike the far more prevalent occurrence of this
168 phenomenon in human HD striatum.
169
170 **mHTT colocalizes with p62, Ub and CTSD in Q175 striatum**
171 Our earlier study in human HD brains (Berg, Veeranna et al. 2024) found a high degree of
172 colocalization of mHTT/Ub or Ub/p62 colocalized signals in IBs, suggesting a relationship
173 between mHTT and the autophagy machinery since p62 and Ub are adaptor proteins mediating
174 autophagic cargo sequestration. Similarly, in Q175 mice, mHTT/Ub or Ub/p62 signals were highly
175 colocalized in IBs, particularly in NIIs, in striatal neurons of Q175 mice (Fig. S1). Additional triple
176 IF labeling experiments (mHTT/Ub/p62) with brain sections from 6- and 10-mo-old Q175 mice
177 identified IBs positive for mHTT, p62 and Ub within or outside the nuclei (Fig. 2A, arrows and
178 arrowheads, respectively). The 10-mo-old Q175 mice exhibited more and larger mHTT-positive
179 IBs than 6-mo mutants (Fig. 2A, 1st column), consistent with Fig. 1A and the literature (Carty,
180 Berson et al. 2015, Deng, Wang et al. 2021). Thus, our data demonstrate a close spatial relationship
181 among mHTT and autophagy receptor protein p62 and Ub in the Q175 model, which is consistent
182 with our observations in human HD brain (Berg, Veeranna et al. 2024).
183 Double IF labeling of mHTT with a LY marker cathepsin D (CTSD) (Fig. 2B1) detected small
184 punctate mHTT signal in CTSD-positive vesicles, suggesting a pool of mHTT within the ALP.
185 Consistent with this light microscopic (LM) finding, IEM with antibody MAB1574 directed
186 against mHTT clearly demonstrated that the AVs in either cell bodies, dendrites and axons were
187 labeled with concentrated silver-enhanced gold particles (Fig. 2B2), and the specificity of the IEM
188 labeling was very high, as reflected by a much higher number of silver-enhanced gold particles
189 associated with AVs versus the minimal number of silver-enhanced gold particles with
190 mitochondria that represent the background labeling (Fig. 2B3). Together, the LM and IEM
191 findings suggest that mHTT molecules exist within ALP vesicles in the absence of definable
192 aggresome/IB structures, similar to the IEM finding from a recent report (Zhou, Peskett et al.
193 2021).
194
195 **Mild late-onset alterations in the ALP revealed in 17-mo-old Q175 mice**
196 We crossed TRGL mice (Lee, Rao et al. 2019) with Q175 to generate TRGL/Q175 and
197 assessed AV/LY subtypes in striatal neurons with a hue angle-based analysis method (Lee, Rao et

198 al. 2019, Lee, Yang et al. 2022). Our pilot studies in young TRGL/Q175 mice (2.5 to 6-mo of age)
199 hardly detected autophagy alterations, compared to the control TRGL mice (not shown). Previous
200 studies have reported that autophagy impairment was hardly detected in 6-mo Q175/GFP-LC3
201 mice (Wold, Lim et al. 2016), but alterations in a limited number of autophagy markers (e.g.,
202 protein levels of p62, LC3, p-Beclin-1) were found in brain homogenates of 12-15-mo Q175 mice
203 (Wold, Lim et al. 2016, Abd-Elrahman, Hamilton et al. 2017, Heikkinen, Bragge et al. 2021).
204 Therefore, to further validate the status of the ALP and to discover potential additional autophagy
205 alterations, we expanded our study to old mice at 17-mo of age, where we found the following
206 ALP alterations.
207
208 ***(1) Alterations in AV/LY subtypes.*** Confocal images from 17-mo-old TRGL/Q175 and control
209 TRGL brain sections, triple-fluorescent labeled via an additional immunostaining with an anti-
210 CTSD antibody and far-red emitting fluorophore, showed enhanced mRFP- and eGFP-LC3 signals
211 in the striatal neurons of TRGL/Q175 compared to TRGL (Fig. 3A1). Hue angle-based analysis
212 confirmed the above observations by revealing significant increases in the numbers of AL and
213 poorly-acidified AL (pa-AL, as explained in Lee et al., 2019; 2022). It also detected a reduction in
214 the number of LY (Fig. 3A2). Thus, these results indicate that the tfLC3 reporter can reveal
215 alterations in the proportions of AV/LY subtypes in Q175, consistent with delayed and/or deficient
216 acidification of AL causing deficits in the reformation of LY to replenish the LY pool.
217
218 ***(2) Mild alterations in the levels of autophagy marker proteins detected by immunoblotting.*** To
219 further assess autophagy phenotypes in Q175 models, we conducted western blotting (WB) using
220 hemibrain homogenates from 17-mo-old mice for protein markers of individual steps in the ALP
221 (i.e., autophagy induction, membrane nucleation/AP formation, autophagy adaptor proteins and
222 AL formation/substrate degradation) (Fig. S2). At the stage of autophagy induction signaling, we
223 did not see alterations in the levels of mTOR and p-mTOR forms including its auto-phospho-form
224 at S2481, but we did observe a decreased level of a mTOR substrate, p-p70S6K (T389), in
225 TRGL/Q175 compared to the control TRGL (Fig. S2A), implying reduced mTOR activity, similar
226 to the finding from a previous study (Ravikumar, Vacher et al. 2004). Another mTOR substrate,
227 p-ULK1 (S757), did not exhibit changes in TRGL/Q175. However, there was an increase in the
228 level of total ULK1, resulting in a reduced ratio of p-ULK1 (S757)/total ULK1 in TRGL/Q175

229 compared to TRGL (Fig. S2A). The data collectively imply a down-regulated mTOR activity, as
230 expected in response to accumulated aggregate-prone protein in Q175 mice, or as a result of
231 sequestration of mTOR by mHTT IBs as suggested previously (Ravikumar, Vacher et al. 2004).
232 Except for these alterations, we did not detect statistically significant differences between
233 TRGL/Q175 and the control TRGL in all other tested marker proteins in the downstream phases
234 of the ALP (Fig. S2B-D). Of special interest is the ATG14-containing VPS34/Beclin-1 complex
235 implicated in HD pathogenesis (Park, Jung et al. 2016, Wold, Lim et al. 2016) for which we did
236 not detect statistically significant alterations in the levels of Beclin-1, VPS34 and ATG14 and their
237 corresponding phosphor-forms. Notably, even if some TRGL/Q175 clearly exhibited diminished
238 signals for p-ATG14 (S29) (Fig. S2B), no statistical significance could be established due to large
239 variations among samples (See Discussion). Another notable point is that we did not find
240 alterations in levels of full-length proteins or fragments (Norman, Cohen et al. 2010, Jamilloux,
241 Lagrange et al. 2018, Sanchez-Garrido, Sancho-Shimizu et al. 2018, Valionyte, Yang et al. 2022)
242 of autophagy adaptor protein such as p62, TRAF6 (Fig. S2C), in contrast to our immunoblot
243 analysis of human HD brains (Berg, Veeranna et al. 2024). Together, our data suggest that, in
244 general, autophagy alterations at the protein level, as can be detected by immunoblotting, are mild
245 in TRGL/Q175 even at 17-mo-old (See Discussion).
246
247 ***(3) Increased numbers of larger lipofuscin granules.*** To assess possible ultrastructural
248 pathologies, we conducted EM study for Q175 vs WT at 17-mo of age. As predicted, NIIs were
249 not observed in WT neurons (Fig. 3B, left panel) but were detected (Fig. 3B, right panel, red circle)
250 in ~10% striatal neurons of Q175 mice. Different from the substantial accumulation of AVs
251 including lipofuscin granules in late stage human HD brain (e.g., HD4) (Berg, Veeranna et al.
252 2024), we did not observe gross accumulation of AVs in Q175 at this old age, except that
253 quantitative analysis of EM images revealed that larger sized (>1 μm) lipofuscin granules (Fig.
254 3B, right panel, arrow) modestly increased in number in Q175 compared to WT [WT: 113
255 lipofuscin/420 neurons (n = 6 mice), i.e., 27 lipofuscin/100 neurons; Q175: 228 lipofuscin/586
256 neurons (n = 9 mice), i.e., 39 lipofuscin/100 neurons; Unpaired t-test, Two-tailed P value < 0.01;
257 Bar graph not shown]. Thus, these EM findings suggest that ultrastructural autophagy alterations
258 in the ALP were mild in Q175 even at an older age.
259

260 **DARPP-32-IR decreases in striatal neurons of 17-mo-old TRGL/Q175 in the absence**
261 **neuronal loss**

262 To investigate potential neurodegeneration in our model, brain sections from 17-mo-old mice
263 were double-labeled with the medium spiny neuron marker DARPP-32 (dopamine- and cAMP-
264 regulated phosphoprotein, 32 kDa)(Ouimet, Langley-Gullion et al. 1998) and a general neuronal
265 marker NeuN. We found that the intensity of DARPP-32-IR significantly diminished in
266 TRGL/Q175 compared to TRGL (Fig. 4A, B). However, there were no alterations in NeuN-IR,
267 including Area Covered and the Number of NeuN-positive neurons (Fig. 4A, B), and there were
268 clear examples of neurons showing strong NeuN signal but faint or no DARPP-32 signal (Fig. 4A,
269 arrows). Such a finding is consistent with other studies in Q175 and Q140 mice where neuronal
270 loss was not found even though a reduction in DARPP-32 was seen in the same study, and that
271 neuronal loss only occurred quite late, e.g., around 2 years of age (Hickey, Kosmalska et al. 2008,
272 Rothe, Deliano et al. 2015, Peng, Wu et al. 2016, Deng, Wang et al. 2021). Thus, our data support
273 the notion that changes in DARPP-32 may indicate alterations in its protein level and a loss of
274 phenotype pattern, which is a potentially common prelude to neuronal loss in other neuronal cell
275 types, e.g., basal forebrain cholinergic neurons (Jiang, Alam et al. 2022).
276

277 **Oral mTORi INK engages mTOR target and induces downstream responses in the ALP in**
278 **7-mo-old TRGL/Q175**

279 As a prelude to investigate effects of pharmacological autophagy stimulation with a mTORi,
280 INK, on TRGL/Q175 mice, we first performed a safety, pharmacokinetic and pharmacodynamic
281 evaluation of INK in 6-mo-old WT mice, administered via oral gavage. The WB results (Fig. S3A)
282 indicated that all doses tested, from 2.5 mg/kg (mpk) to 10-mpk, exhibited target engagement as
283 revealed by the reductions in the protein levels of mTOR targets, i.e., p-ULK1 (S757,
284 phosphorylated by mTOR), p-p70S6K (not shown) or phosphorylated S6 ribosomal protein (p-S6,
285 at S240/244), implying high BBB permeability of this compound and target engagement.
286 Consistently, measurements for the levels of INK in cerebellar homogenates of WT mice treated
287 with 1, 3 and 10-mpk INK revealed dose-dependent brain levels of INK (Fig. S3B).

288 We then decided an oral gavage treatment regimen for INK as 4-mpk, daily, for 3 weeks, to be
289 administered in 6-mo-old TRGL/Q175. The brains from the mice (7-mo of age after the 3-week
290 treatment duration) were then analyzed by multiple experimental approaches. By immunoblotting,

291 target engagement was verified, as indicated by decreased levels of p-mTOR (S2481,
292 autophosphorylation site), p-ULK1 (S757) and p-S6 (S240) in brain homogenates from INK-
293 treated TRGL/Q175 compared to Veh-treated TRGL/Q175 (Fig. 5A, B). Additionally, there were
294 also INK induced changes in marker proteins located downstream of autophagy induction,
295 including, for example, increased levels of p-ATG14 in INK-treated samples (Fig. 5A, B). It is
296 interesting that although INK did not induce any alterations in the transgene product tfLC3-I or -
297 II, there was a trend of decreased endogenous LC3-I, leading to a statistically significant increase
298 in the ratio of LC3-II/I, and such a result in LC3-I reduction was reproduced in a repeated
299 experiment (Fig. 5A, B). Thus, the pilot study in WT mice and the actual study in TRGL/Q175
300 mice together established mTORi INK's BBB permeability, target engagement and ability to
301 modify molecular events in the ALP.
302
303 **mTOR inhibition alters AV/LY subtypes**
304 We took advantage of the tfLC3 construct reporting *in vivo* autophagy flux (Lee, Rao et al.
305 2019) to assess INK effects on AV/LY subtypes in TRGL/Q175. Confocal images from INK- or
306 Veh-treated TRGL/Q175 and Veh-treated TRGL brain sections of 7-mo-old mice, immuno-
307 stained with anti-CTSD antibody and detected with a third fluorophore, were collected (Fig. 6A)
308 and processed for hue-angle based quantitative analysis using the protocol described previously
309 (Lee, Rao et al. 2019). The analysis in striatal neurons (Fig. 6B) revealed reversal of the two main
310 ALP alterations. First, the pre-existing abnormally lowered LY number in TRGL/Q175-Veh (Fig.
311 6B, LY group, red vs green), was reversed by INK treatment (Fig. 6B, LY group, red vs blue).
312 Second, INK reduced the number of AL in TRGL/Q175-Veh compared to TRGL-Veh (Fig. 6B,
313 AL group, red vs blue), implying improved AL clearance and likely providing the basis for
314 restoration of normal LY number. Together, the data suggest that autophagy phenotype in 7-mo
315 Q175 is measurable but milder than that in the 17-mo-old mice shown in Fig. 3A and that INK has
316 the potential to modulate the autophagy pathway and restore normal function at this mild disease
317 stage.
318
319 **mTOR inhibition mitigates mHTT-related aggresome pathology**
320 Importantly, we found that HD-like pathology such as mHTT IBs and associated protein
321 aggregation of adaptor proteins, p62 and Ub, was ameliorated by INK treatment. Confocal images

322 demonstrated that mHTT positive particles/inclusions were substantially reduced in INK-treated
323 7-mo-old TRGL/Q175, compared to Veh-treated TRGL/Q175 mice (Fig. 7A). Moreover, p62-IR
324 or Ub-IR also changed in a similar trend (Fig. 7A), consistent with the high degree of colocalization
325 of mHTT/p62/Ub signals shown in Fig. 2A. The corresponding quantitative analysis, shown as
326 Area Covered by either mHTT-, p62- or Ub-IR on a per cell basis, confirmed statistically
327 significant decreases in the Total Area Covered by mHTT-, p62-signals (Fig. 7B1). With the
328 assistance of the endogenous tfLC3 signal (particularly the mRFP signal) in the TRGL to identify
329 the association status of the mHTT-, p62- or Ub-IR with AVs, the images were additionally
330 quantified to generate the separated "Area Covered by the AV-associated Form" (Fig. 7B2) and
331 "Area Covered by the AV-unassociated Form" (Fig. 7B3) of mHTT-, p62- or Ub- signals. The
332 results collectively suggest decreased mHTT-, p62- or Ub-IR in treated compared to untreated
333 TRGL/Q175, implying that INK treatment was able to promote the clearance of mHTT and related
334 receptor proteins p62 and/or Ub.
335
336 **mTOR inhibition does not reverse preexisting DARPP-32-IR reduction in TRGL/Q175**
337 Finally, we evaluated neurodegenerative changes by employing DARPP-32 IHC on brain
338 sections of Veh-treated or INK-treated TRGL/Q175. Similar to what was found in 17-mo-old mice
339 (Fig. 4), the group of TRGL/Q175-Veh, even at this young age (7-mo), already exhibited a
340 diminished DARPP-32-IR signal compared to that in TRGL-Veh (Fig. 8A, B). However, no
341 differences between the untreated and INK-treated TRGL/Q175 groups were established by
342 quantitative analysis (Fig. 8A, B). Thus, the result suggests a lack of effectiveness of INK in
343 reversing this pre-existing phonotype, implying that earlier intervention may be necessary
344 (Marchionini, Liu et al. 2022).
345
346
347 **DISCUSSION**
348 Previous studies in cell and animal models have documented roles of HTT and mHTT in
349 autophagy in relation to HD (Martin, Ladha et al. 2015, for reviews, see Croce and Yamamoto
350 2019, Klionsky, Petroni et al. 2021). WT HTT participates in normal autophagy by releasing
351 ULK1 via mTOR inhibition and serving as a scaffold to facilitate cargo sequestration by enhancing
352 p62 interaction with LC3 and ubiquitinated cargos (Ochaba, Lukacsovich et al. 2014, Rui, Xu et

353 al. 2015). mHTT in HD may activate autophagy by sequestering and thus inhibiting mTOR
354 (Ravikumar, Vacher et al. 2004). Most mHTT effects in cellular and mouse HD models appear to
355 be inhibitory for autophagy induction steps, from initiation signaling and phagophore nucleation
356 to cargo recognition/AP formation (Martinez-Vicente, Talloczy et al. 2010, Pryor, Biagioli et al.
357 2014, Rui, Xu et al. 2015, Wold, Lim et al. 2016, Ashkenazi, Bento et al. 2017). In addition, mHTT
358 may disturb endolysosomal homeostasis by reducing exocytosis and promoting AL accumulation
359 (Zhou, Peskett et al. 2021). In the current study using Q175, we have found that mHTT is an ALP
360 substrate and that the ALP is relatively intact, with some late-onset minor alterations, such as
361 insufficient mTOR activity reflected by lowered phospho-p70S6K level and ratio of phospho-
362 ULK1 (S757)/total ULK1, lysosome depletion and AL/pa-AL elevation. This mild late-onset
363 nature of ALP pathogenesis allowed us to modulate ALP with a mTOR inhibitor in 6-mo-old
364 TRGL/Q175 which resulted in positive effects on rescuing Q175 phenotypes including
365 normalization of AL/LY subtypes and reduction in aggresome pathology.
366
367 **ALP impairments in Q175 are mild and late-onset**
368 In the current study, we assessed ALP alterations in the Q175 model by analyzing protein
369 markers in all phases of the ALP including autophagy induction signaling, membrane
370 nucleation/AP formation, autophagy adaptor proteins and AL formation/substrate degradation. By
371 immunoblot analysis, alterations in the tested marker proteins even at 17 months of age in
372 TRGL/Q175 mice were limited to a reduction in p-P70S6K (T389), similar to that reported
373 previously (Ravikumar, Vacher et al. 2004), and a reduced ratio of p-ULK1 (S757)/total ULK1
374 as a result of increased total ULK1. While these two alterations together would suggest a lower
375 mTOR activity and autophagy activation, consequential alterations of downstream markers,
376 particularly proteins in the ATG14-containing Beclin-1/VPS34 complex, were not detected.
377 Although 4 out of the 10 tested TRGL/Q175 mice exhibited very low levels of p-ATG14, implying
378 a deficit in this complex as previously reported (Wold, Lim et al. 2016), variation among animals
379 was too great to draw statistical conclusions. In this regard, mice used in the current study were
380 heterozygous, which results in less autophagy alteration than that reported in homozygous mice
381 using certain autophagy markers (Abd-Elrahman, Hamilton et al. 2017). It may also be noted in
382 our experience that immunoblot analysis of brain tissue averages contributions from varied cell
383 types that may respond to disease states in opposite directions and mask changes in a given cell

384 population. Thus, we also applied a neuron-specific analysis using our neuron-specific tfLC3
385 reporter and hue-angle based image quantification approach, which yielded more sensitive
386 detection and findings.

387 In brain sections from 17-mo-old TRGL/Q175 mice, we observed increased numbers of AL
388 including the population of pa-AL and reduced numbers of LY. Such changes in AL/pa-AL were
389 not readily observed in TRGL/Q175 mice at 2 months (not shown) or 7 months (e.g., Fig. 6B,
390 which only exhibited a reduction in LY number) of age, indicating that even if these alterations
391 signify an existence of impairments in the late phase of the ALP, they do not occur until a later
392 age (e.g., 17 mo). Importantly, this pattern of late-onset ALP pathology progression, e.g., AL/pa-
393 AL increases, is consistent with our findings from HD human brains (Berg, Veeranna et al. 2024)
394 where enlarged CTSD-positive AL accumulate and cluster in affected neuronal populations at the
395 late disease stages (HD3 and HD4). These findings suggest that the overall autophagy function in
396 heterozygous Q175 is largely maintained until the relatively late disease stage and provide a
397 rationale to stimulate autophagy as a therapeutic intervention when the autophagy machinery is
398 still functional, which would generate beneficial effects. We obtained support for this concept in
399 the subsequent study with mTORi INK when administered to TRGL/Q175 at 6 months of age for
400 three weeks.

401

402 **Autophagy as a primary mechanism for INK-enhanced clearance of small mHTT species**

403 One of the key findings from this study is the reduction of mHTT-IR in neurons detected by
404 immunolabeling after the 3-week oral treatment with mTORi INK (Fig. 7). This beneficial
405 outcome from the drug treatment is interpreted as a primary result of the manipulation/stimulation
406 of autophagy by the compound, leading to enhanced autophagy clearance of mHTT species
407 including smaller, presumably soluble, species and larger aggregates such as the IBs. This
408 interpretation is supported by the following considerations and evidence. First, in theory, the
409 compound used for the treatment is a mTORi so is expected to enhance autophagy (Kim and Guan
410 2015, Bensalem, Fourrier et al. 2021). Second, target engagement is achieved as clearly reflected
411 by the diminished levels of mTOR-mediated phosphorylation on mTOR itself (S2481), ULK1
412 (S757) and p-S6 (S240/S244), along with changes in proteins downstream of mTOR, such as p-
413 ATG14 (S29) and LC3. Third, hue-angle based confocal image analysis of AL/LY subtypes
414 reveals a reduced AL number and an increased LY number in INK-treated TRGL/Q175 compared

415 to Veh-treated TRGL/Q175. The findings from this analysis of AL/LY subtypes highlights the
416 advantages of crossing TRGL with Q175 mice to evaluate autophagy modulators on the ALP,
417 consistent with a notion of developing better tools capable of investigating autophagy flux *in vivo*
418 (Nixon 2013, Vodicka, Lim et al. 2014).

419 Our confocal microscopy analyses revealed mHTT signal in CTSD-positive vesicles, which
420 can be classified as AL based on their LC3 fluorescence, and IEM detected mHTT-silver-enhanced
421 gold particles in AP and AL including lipofuscin granules. Both findings indicate the existence of
422 mHTT species inside the ALP as autophagy substrates. The presence of low levels of mHTT in
423 CTSD-positive AL also implies a constitutive functional degradation event of mHTT in AL (Fig.
424 2B1, 10-mo-old mouse). This is in contrast to the case in young AD mouse models where early-
425 onset autophagy-stress exhibited severe substrate accumulation (e.g., reflected by strong LC3
426 signal) due to deficits of degradative functions within AL. (Lee, Yang et al. 2022). A reduced level
427 in the portion of AV-associated mHTT signals (Fig. 7B2) by mTORi INK further suggests that
428 mHTT degradation has been enhanced after manipulating the ALP. This AV-associated mHTT
429 pool is considered to be corresponding to the mHTT-silver-enhanced gold signal under IEM (Fig.
430 2B2), i.e., amorphous and existing within the lumen of AV. Such mHTT localization and
431 ultrastructural features are consistent with recent findings that mHTT proteins exogenously added
432 to Q175 brain sections for incubation are recruited to multivesicular bodies/amphisomes, AL and
433 residual bodies (lipofuscin granules), and ultrastructurally localized to non-fibrillar, electron-
434 lucent regions within the lumen of these organelles (Zhou, Peskett et al. 2021).

435

436 **Possible autophagy-related mechanism for the clearance of large mHTT IBs**

437 It is notable that the AV-non-associated form of mHTT (i.e., did not show colocalization with
438 the endogenous tfLC3 signal implying that they might not have a contact with AVs) decrease more
439 obviously after drug-treatment, along with the reductions in p62 and Ub signals (Fig. 7B3). These
440 mHTT species are mainly larger aggresomes/IBs, including those within the nuclei. Based on our
441 mHTT-IEM observation (Fig. 1B), the IBs in Q175 brain are fibrillar aggregates in the nucleus
442 and cytoplasm, exhibiting a homogeneous feature in shape (i.e., round/oval cotton-ball) and in
443 content (i.e., short fine fibrils), similar to the nuclear IBs we found in human HD brains (Berg,
444 Veeranna et al. 2024), whose cytoplasmic and neuritic IBs, however, also exhibit more
445 heterogeneous compositions such as a mixture of fine fibrils with AVs, fingerprint-like structures

446 or bundles of microtubules. In the current study, we did not observe that a whole IB is contained
447 within an AP or AL in our EM examination, raising a question of how these larger aggregates
448 could be degraded by the autophagy machinery after an autophagy activation by mTOR inhibition.
449 This issue is informed by findings that the mHTT species are dynamic and the aggregates can form
450 as different phases (liquid-like or solid-like), making it possible for mHTT species to move out or
451 into IBs (Liu, Shyu et al. 2015, Peskett, Rau et al. 2018, Aktar, Burudpakdee et al. 2019, Riguet,
452 Mahul-Mellier et al. 2021) and to shuttle between the nucleus and the cytoplasm (Xia, Lee et al.
453 2003, Atwal, Xia et al. 2007). Thus, it is speculated that under the autophagy activated condition
454 induced by mTOR inhibition, the enhanced clearance of mHTT in the ALP pool would promote
455 movements of mHTT species from the IB forms, leading to a reduction on the overall mHTT load.
456

457 **UPS as an additional mechanism for the clearance of mHTT species**

458 Even if INK is a mTORi mainly targeting autophagy, we cannot completely exclude additional
459 contributions from the UPS for the observed reduction of mHTT species given the crosstalk
460 between the two proteolytic systems. It is well accepted that autophagy plays a more important
461 role in the clearance of larger protein aggregates such as aggresomes/IBs (Sarkar and Rubinsztein
462 2008). For example, autophagy is involved in the degradation of p62 bodies (Bjørkøy, Lamark et
463 al. 2005) and autophagy markers are colocalized with cytoplasmic mHTT IBs (Iwata, Christianson
464 et al. 2005). However, there is also evidence for degradation of polyQ aggregates in the nuclei
465 (Iwata, Nagashima et al. 2009), which contain p62 condensates as a hub for UPS-mediated nuclear
466 protein turnover (Fu, Cohen-Kaplan et al. 2021). We observed a high level of colocalization of
467 mHTT with p62 and Ub in aggregates at both intranuclear and extranuclear locations (Fig. 2A),
468 which is presumably more related to the UPS hub and autophagy, respectively. It is possible that
469 stimulation of autophagy is reducing the mHTT in the cytoplasm and thereby partially relieves the
470 burden of the proteasome both in the cytoplasm and in the nucleus so that the nuclear proteasome
471 operates more effectively.
472

473 In summary, Q175 models, as detected in the current study, develop ALP alterations late in the
474 disease progression. Although milder than what is seen in late-stage HD human brain (Berg,
475 Veeranna et al. 2024), there are similarities in ALP pathobiology between human HD brains and
476 Q175 brains. These include late-onset nature, mHTT as an ALP substrate, increased AL/pa-AL,

477 mouse IB ultrastructural feature similar to the common fine fibril type of human IBs. The late-
478 onset mild ALP pathology in Q175 is different from the severe AV accumulation in mouse models
479 of AD as mentioned above (Lee, Yang et al. 2022). Together, the mild and late-onset nature of
480 ALP alterations in Q175 provides a basis for manipulating autophagy to be a promising therapeutic
481 strategy if the manipulations (e.g., stimulating autophagy with mTORi as in this study) are applied
482 when the autophagy machinery is largely undamaged. This has been validated to be successful in
483 this study as demonstrated by the INK-induced reduction of mHTT species along with other
484 beneficial effects, consistent with findings from similar studies and supporting the general notion
485 of lowering mHTT as a therapeutic strategy for HD (Cortes and La Spada 2014, Barker, Fujimaki
486 et al. 2020).
487

ACKNOWLEDGMENTS

This work was supported by the CHDI Foundation (R.A.N.) and the National Institute of Aging (P01 AG017617 to R.A.N.). We are grateful to Dr. T Yoshimori (Osaka University, Japan) for the mRFP-eEGFP-LC3 construct used in the TRGL mice.

CONFLICT OF INTEREST STATEMENT

All authors declare no conflict of interests.

497 **FIGURE LEGENDS**

498 **Fig. 1. Identification of inclusions and HTT molecular species in Q175 mice.**

499 ***(A) IHC detects age-dependent increase in the number of mHTT inclusions.*** Brain sections from
500 6-mo- and 10-mo-old WT and Q175 mice were processed for IHC with antibody mEM48
501 (MAB5374) directed against mHTT (A). Images from sections without (A1-3) or with (A4) a
502 cresyl violet counterstain are shown where the dark-brown puncta represent mHTT-positive
503 inclusions. Arrowheads depict neuronal intranuclear inclusions (NIIs), determined with the
504 assistance from the nuclear labeling by cresyl violet, while arrows indicate extranuclear inclusions,
505 primarily the neuritic inclusion in the neuropil. Bars = 20 μm.

506 ***(B) mHTT inclusions are detected in nucleus, dendrites and axons of Q175 brains by IEM.***
507 Sagittal vibratome brain sections of 17-mo-old Q175 were cut and went through EM processing.
508 Small blocks were obtained from the striatal areas for ultrathin sectioning. Tissue containing grids
509 were processed for immunogold labeling procedure with antibody mEM48, using 10 nm gold
510 followed by silver enhancement. Structures showing high level of silver-enhanced gold labeling
511 were considered as mHTT-positive.

512 ***(C) Various forms of HTT molecules are detected with different antibodies by immunoblotting.***
513 Equal amounts of proteins from hemibrain homogenates of 17-mo-old WT, TRGL, Q175 and
514 TRGL/Q175 (labeled as "Cross") were subjected to SDS-PAGE and processed for WB with
515 different antibodies directed against HTT/mHTT, including MAB1574 (C1, C2), mAb PHP2 (C1)
516 and MAB5490 (C2). Images were collected by a digital gel imager (Syngene G:Box XX9). The
517 arrowhead and arrow (C2) depict a 120 kDa and a 48 kDa fragment, respectively. (C3)
518 Densitometry was performed with Image J for the blots shown in (C2) and the results were
519 normalized by the immunoblot(s) of given loading control protein(s) (e.g., GAPDH). Values are
520 the Mean +/- SEM for each group (n = 7 TRGL, 4 Q175 and 10 TRGL/Q175). Significant
521 differences among the groups were analyzed by One-Way ANOVA followed by Sidak's multiple
522 comparisons test. * $P < 0.05$, ** $P < 0.01$.

523

524 **Fig. 2. Colocalization of mHTT with p62, Ub and CTSD.**

525 ***(A) Triple labeling detects colocalization of mHTT with both autophagy adaptor proteins p62***
526 ***and Ub.*** Brain sections from 6-mo- and 10-mo-old mice were immunostained with antibodies to
527 HTT (antibody MW8; red), p62 (green) or pan-Ub (blue), followed by an additional DAPI (cyan)

528 labeling, and confocal images from the striatum are shown. Boxed areas are enlarged and shown
529 in the last column. Arrows and arrowheads depict the white areas representing triply labeled
530 inclusions containing the signals of the three proteins, where arrows are for NIIs, determined with
531 the assistance from the nuclear DAPI labeling, while the arrowheads are for extranuclear
532 inclusions. Bar = 10 μm.
533 ***(B) mHTT is detected in vesicles of the ALP.*** (B1) Brain sections from 10-mo-old Q175 were
534 double-immunolabeled with antibodies to HTT (antibody MW8; green) and CTSD (red), followed
535 by an additional DAPI (blue) labeling, and a 3-color-merged confocal image from the striatum is
536 shown. Large and small green arrows depict HTT nuclear and extranuclear inclusions,
537 respectively, while yellow arrowheads depict yellow puncta showing HTT and CTSD signal
538 colocalization. Bar = 10 μm. (B2) IEM with anti-HTT antibody (MAB1574) specifically detects
539 HTT signal, represented by the silver-enhanced gold particles (red arrowheads), in AV/LY in cell
540 bodies, dendrites and axons. (B3) To demonstrate the labeling specificity of the HTT antibody in
541 this IEM study, the number of silver-enhanced gold particles in AV/LY existing in neuronal cell
542 bodies and neurites was counted from 69 EM images from two 10-mo-old Q175 mice against the
543 number of silver-enhanced gold particles in mitochondria on the same images, and the result is
544 shown in the bar graph. Statistical significances between the two groups were analyzed by
545 unpaired, two-tailed t-test. **** $P < 0.0001$.
546
547 **Fig. 3. Mild late-onset alterations in the ALP in the striatum of 17-mo-old Q175.**
548 ***(A) Quantitation of AV/LY subtypes of striatal neurons detect increases in AL, pa-AL and a***
549 ***decrease in LY in 17-mo-old TRGL/Q175 vs. TRGL.*** (A1) Brain sections from TRGL and
550 TRGL/Q175 (4 sections/mouse, 10 mice/genotype) were immunostained with an anti-CTSD
551 antibody. Confocal images from the cranial-dorsal portion of the striatum (3 images at
552 120x/section) were collected and representative images for each eGFP-LC3 (green), mRFP-LC3
553 (red) and CTSD (blue) are shown. Arrowheads depict pa-AL. (A2) Hue angle-based analysis was
554 performed for AV/LY subtype determination using the methods described in Lee et al., 2019. Data
555 are presented as Vesicle #/Neuron (TRGL: n = 713 neurons; TRGL/Q175: n = 601 neurons).
556 Statistical significances between the two groups for each vesicle type were analyzed by unpaired
557 t-test. Two-tailed P value: *** $P<0.001$, **** $P<0.0001$.

558 ***(B) EM detects larger AL/lipofuscin granules in the Q175 striatum.*** Sagittal vibratome brain
559 sections from 17-mo-old mice were cut and went through EM processing. Small blocks were
560 obtained from the striatal area for ultrathin sectioning, followed by EM examinations of the grids.
561 The red circle depicts NII, and the arrow depicts larger sized (> 1μm) lipofuscin granules, which
562 were counted on randomly collected images of neurons from striatum of WT (420 neurons from n
563 = 6 mice) or Q175 (586 neurons from n = 9 mice).
564
565 **Fig. 4. Decrease of DARPP-32-IR in striatal neurons of 17-mo-old TRGL/Q175 in the**
566 **absence of a NeuN signal reduction.**
567 Brain sections from TRGL and TRGL/Q175 (n = 10 mice/genotype, 4 sections/mouse) were
568 double-immunostained with anti-DARPP-32 and -NeuN antibodies. Confocal images from the
569 cranial-dorsal portion of the striatum (3 images at 120x/section) were collected and representative
570 images are shown (A). Arrows depict examples of neurons showing strong NeuN signal while
571 minimal DARPP-32-IR. (B) Images were quantified by Image J for Integrated Density of DARPP-
572 32- (top) or NeuN-IR/Image field (middle), and for # of NeuN positive cells/Image field (bottom).
573 Statistical significances between the two groups were analyzed by unpaired, two-tailed t-test. * P
574 < 0.05.
575
576 **Fig. 5. mTORi INK exhibits target engagement and induces downstream responses in the**
577 **ALP in 7-mo-old TRGL/Q175.**
578 Equal amounts of proteins from brain homogenates of 7-mo-old TRGL/Q175 mice untreated
579 (labeled as "Veh") or mTORi INK treated [4 mg/kg (4-mpk), daily, 3 weeks; labeled as "INK"]
580 were subjected to SDS-PAGE and processed for WB with antibodies directed against several
581 marker proteins in the autophagy pathway, representing target engagement of INK or downstream
582 responses. Representative blots are shown on the left (A) while quantitative results of the blots are
583 shown on the right (B). The bottom LC3 blots represent a repeated immunoblotting experiment.
584 Values are the Mean +/- SEM for each group (n = 6-7 mice per condition). Significant differences
585 between the two groups were analyzed by unpaired, two-tailed t-test. * P<0.05, ** P<0.01, ***
586 P<0.001, **** P<0.0001. tfLC3 = mRFP-eGFP-LC3; Endo-LC3 = endogenous LC3.
587

588 **Fig. 6. mTORi INK reverses the mild alteration of AV/LY subtypes in the striatum of 7-mo-**
589 **old TRGL/Q175.**
590 (A) Brain sections from untreated or INK (4-mpk, 3w)-treated TRGL/Q175 vs. TRGL (4
591 sections/mouse, 5-6 mice per condition) were immunostained with an anti-CTSD antibody.
592 Confocal images from the cranial-dorsal portion of the striatum (3 images at 120x/section) were
593 collected and representative images for each eGFP-LC3 (green), mRFP-LC3 (red) and CTSD
594 (blue) are shown. (B) Hue angle-based analysis was performed for AV/LY subtype determination
595 using the methods described in Lee et al., 2019. Data are presented as Vesicle #/Neuron (TRGL-
596 Veh: n = 260 neurons; TRGL/Q175-Veh: n = 218 neurons; TRGL/Q175-INK: n = 287 neurons).
597 Statistical significances among the groups were analyzed by One-Way ANOVA followed by
598 Sidak's multiple comparisons test. ** P<0.01, **** P<0.0001.
599
600 **Fig. 7. mTORi INK reduces HTT-, Ub- or p62-IR-covered areas parallelly in the striatum of**
601 **7-mo-old TRGL/Q175.**
602 (A) Brain sections from INK (4-mpk, 3w)-treated or untreated TRGL/Q175 (4 sections/mouse, 6-
603 7 mice/condition,) were immunostained with anti-HTT (MW8), -p62 or -pan-Ub antibodies.
604 Confocal images from the cranial-dorsal portion of the striatum (3 images at 120x/section) were
605 collected. Shown are single-channel images (i.e., without showing the eGFP and mRFP signals).
606 (B1-B3) Areas covered by either the HTT-, p62- or Ub-IR on a per cell basis are quantified (for
607 HTT-IR, TRGL/Q175-Veh: n = 196 neurons, TRGL/Q175-INK: n = 385 neurons; for p62-IR,
608 TRGL/Q175-Veh: n = 311 neurons, TRGL/Q175-INK: n = 378 neurons; for Ub-IR, TRGL/Q175-
609 Veh: n = 244 neurons, TRGL/Q175-INK: n = 347 neurons) and grouped as "Total Area" (B1),
610 "AV-associated Form" (i.e., the IR which was associated with tfLC3 signals representing
611 AVs)(B2) or "AV-unassociated Form" (i.e., the IR which was not associated with the tfLC3
612 signals)(B3). Statistical significances between the two groups were analyzed by unpaired t-test.
613 Two-tailed P value: * P < 0.05, **** P < 0.0001.
614
615 **Fig. 8. INK treatment does not reverse the reduction of DARPP-32-IR in the striatum of 7-**
616 **mo-old TRGL/Q175.**
617 (A) Sagittal brain sections containing the striatum area were immunostained with an anti-DARPP-
618 32 antibody, and 10x images taken from the cranial-dorsal portion of the striatum are shown (1st

619 row). Boxed areas on the 1st row are enlarged and shown on the 2nd row for easy viewing of the
620 immunostaining patterns for each condition. (B) For quantitation purpose, each whole 10x image
621 (excluding the areas covered by the fiber bundles which usually exhibited minimal background
622 staining – achieved by threshold setting) was quantified by Image J (1 image/section, 4
623 sections/mouse) and the results are expressed as the Integrated Density of DARPP-32-IR. n = 6-8
624 mice/condition. Statistical significances among the groups were analyzed by One-Way ANOVA
625 followed by Sidak's multiple comparisons test. ** $P < 0.01$ compared to TRGL-Veh.
626

627 **SUPPLEMENTAL FIGURE LEGENDS**

628 **Fig. S1 (related to Fig. 2): Colocalization of HTT/Ub and Ub/p62 in IBs in the STR.**

629 Brain sections from 10-mo-old mice were processed for double IF with antibodies against HTT
630 (antibody MW8; red) and pan-Ub (green), or pan-Ub (red) and p62 (green), and confocal images
631 from the striatum are shown. Arrowheads depict IBs showing colocalization signals.

632

633 **Fig. S2 (related to Fig. 3): Molecules involved in various stages of the ALP are largely**
634 **unchanged in 17-mo-old TRGL/Q175.**

635 Equal amounts of proteins from brain homogenates of 17-mo-old TRGL and TRGL/Q175 were
636 subjected to SDS-PAGE and processed for WB with antibodies directed against a number of
637 interested marker proteins in the ALP, grouped according to the functions of the proteins in the
638 autophagy process: autophagy induction signaling (A), membrane nucleation/AP formation (B),
639 autophagy adaptor proteins (C) and AL formation/substrate degradation (e.g., lysosomal
640 hydrolases or structural components)(D). The blot of the loading control protein GAPDH is boxed
641 and placed under each protein of interest. Images were collected by a digital gel imager (Syngene
642 G:Box XX9). Densitometry was performed with Image J and the result for each protein of interest
643 was normalized by its corresponding GAPDH blot and presented in the bar graph. Values are the
644 Mean +/- SEM for each group (n = 7 TRGL and 10 TRGL/Q175). Significant differences between
645 the 2 groups were analyzed by unpaired, two-tailed t-test. * $P < 0.05$, ** $P < 0.01$, *** $P < 0.001$.

646

647 **Fig. S3 (related to Fig. 5): Dosing tests demonstrate mTORi INK BBB penetration and target**
648 **engagement even at low dosages.**

649 ***(A) Dosing tests for INK.*** INK or the vehicle was administered by oral gavage. Two dosing tests
650 were done in 6-mo-old WT mice, one with 10, 8 mg/kg (mpk) every other day or 4-mpk daily for
651 2 weeks and the other with 7.5, 5, 2.5-mpk daily for 2 weeks. Equal amounts of proteins from brain
652 homogenates of mice receiving vehicle (labeled as "Veh") or INK were subjected to SDS-PAGE
653 and processed for WB with antibodies directed against marker proteins representing target
654 engagement of INK, such as p-ULK1 (S757) and p-S6 – the drug effects are reflected by the
655 changes within the boxed areas compared to the signals of Veh outside the boxed areas.

656 ***(B) INK was detected in the brains of mice receiving a single dose via oral gavage.*** After 6, 12
657 or 24 hrs post INK administration to 6-mo-old WT mice, INK was detected in cerebellum of mice

658 treated with 1, 3 or 10-mpk INK. Total 60 mice: n = 6 mice/dose/time point, where the Vehicle
659 control group was just tested once at the 6-hr time point.
660

661 **MATERIALS AND METHODS**

662 ***The HD Q175 mouse model and the generation of a new Q175 model crossed with the autophagy***
663 ***reporter mouse TRGL (TRGL/Q175)****:* Q175 mice (B6J.zQ175 Knock-In mice, CHDI-
664 81003003)(Menalled, Sison et al. 2003, Menalled, Kudwa et al. 2012) were obtained from the
665 Jackson Lab (Stock No. 027410) on a C57BL/6J background. The zQ175 KI allele has the mouse
666 *Htt* exon 1 replaced by the human *HTT* exon 1 sequence containing a ~190 CAG repeat tract, and
667 the average size for the mice used in this study was 200 CAG. Q175 genotyping and CAG sizing
668 were conducted by Laragen, Inc. (Culver City, CA). The TRGL (**T**hy-1 m**R**FP-e**G**FP-**L**C3) mouse
669 model, expressing tandem fluorescence-tagged LC3 (tfLC3 or mRFP-eGFP-LC3) in neurons, was
670 generated, genotyped by PCR and maintained in a C57BL/6J background as described previously
671 (Lee, Rao et al. 2019). The TRGL was crossed with Q175 to generate the new TRGL/Q175 model
672 featuring the tfLC3 probe as an *in vivo* autophagy reporter.

673 The mice were maintained in the Nathan Kline Institute for Psychiatric Research (NKI) animal
674 facility and housed in a 12 hrs light/dark cycle. All animal procedures were performed following
675 the National Institutes of Health Guidelines for the Humane Treatment of Animals, with approval
676 from the Institutional Animal Care and Use Committee at the NKI. Animals of both sexes were
677 used in this study. Details for mouse ages are in the Figure Legend and/or Results. All efforts were
678 made to minimize animal suffering and number of animals used.

679

680 ***mTORi INK administration to mice****:* INK-128 (ChemScene) was formulated in the sterile filtered
681 vehicle (Veh) – 0.5% carboxymethyl cellulose (Sigma, Cat #5678) and 0.05% tween 80 in water
682 – at different concentrations to achieve the various desired dosages. The mixture was homogenized
683 with a tissue homogenizer, stored in a sterile container at room temperature for up to 2 weeks, and
684 stirred prior to each dosing. It was administered to mice via oral gavage at a dose volume of 5
685 ml/kg, which was a relatively smaller volume of drug solution (generally 100-150 ul depending
686 on the mouse body weight) aimed at avoiding the suppression of appetite. Mice receiving the Veh
687 (also at a solution volume of 5 ml/kg) served as the control group. Oral gavage was conducted
688 with 20G-38mm Cadence Science™ Malleable Stainless-Steel Animal Feeding Needles #9921
689 (Fisher Sci Cat #.14-825-275).

690

691 ***mTORi INK pharmacokinetics in mouse brains after oral administration:*** INK was formulated
692 into 0.5% carboxymethyl cellulose and 0.05% tween-80 in water to be administered orally. 6
693 months old C57B6/J male mice were treated with compound at 1, 3 or 10 mg/kg (mpk) or vehicle.
694 6, 12 or 24 hours after administration, mice were terminally anesthetized with pentobarbital and
695 cerebellum was dissected and fresh frozen on liquid nitrogen and stored at -80ºC until analysis.
696 Tissue was homogenized and extracted with acetonitrile (containing 0.1% formic acid). Extract
697 was analyzed using a LC-MS/MS (Waters Xevo TQ MS) method with a lower limit of quantitation
698 of 13 nM.
699
700 ***Brain tissue preparation****:* To obtain tissues for experiments, the animals were anesthetized with a
701 mixture of ketamine (100 mg/kg BW) and xylazine (10 mg/kg BW). Mice for light microscopic
702 (LM) analyses were usually fixed by cardiac perfusion using 4% paraformaldehyde (PFA) in 0.1
703 M sodium cacodylate buffer [pH 7.4, Electron Microscopy Sciences (EMS), Hatfield, PA].
704 Following perfusion fixation, the brains were immersion-fixed in the same fixative overnight at
705 4°C. For transmission electron microscopic (EM) study, 4% PFA was supplemented with 2%
706 glutaraldehyde (EMS). For biochemical analyses such as immunoblotting, the brains were flash
707 frozen on dry ice and stored at –70°C. When both morphological and biochemical analyses were
708 to be performed on the same brain, the brain was removed after brief perfusion with saline. One
709 hemisphere was frozen at –70°C and the other half was immersion-fixed in 4% PFA for 3 days at
710 4°C.
711
712 ***Antibodies for immunohistochemistry (IHC) and western blotting (WB):*** The following primary
713 antibodies were used in this study. <u>(1) from Cell Signaling Technology:</u> tHTT rabbit mAb (total
714 HTTs, #5656), MTOR rabbit mAb (#2983); p-MTOR (S2481 autophosphorylation) pAb (#2974),
715 p-MTOR (S2448) pAb (#2971), p70S6K rabbit mAb (#2708), p-p70S6K (S371) pAb (#9208), p-
716 p70S6K (T389) rabbit mAb (#9235), S6 ribosomal protein mAb (#2317), p-S6 ribosomal protein
717 (S240/244) rabbit mAb (#5364), ULK1 pAb (#4773), ULK1 rabbit mAb (#6439), p-ULK1 (S757)
718 pAb (#6888), p-ULK1 (S317) pAb (#37762), ATG5 rabbit mAb (#12994), ATG14 pAb (#5504),
719 p-ATG14 (S29) rabbit mAb (#92340), p-Beclin 1 (S30) rabbit mAb (#35955), VPS34 rabbit mAb
720 (#4263), TRAF6 rabbit mAb (#8028). <u>(2) from Millipore-Sigma:</u> ntHTT mAb (mEM48,
721 #MAB5374; N-Terminus-specific), HTT mAb (1C2, #MAB1574; epitope: N-terminal part of the

722 human TATA Box Binding Protein (TBP) containing a 38-glns stretch), HTT mAb (#MAB5490;
723 epitope: human HTT aa115-129), ATG5 pAb (#ABC14), LC3 pAb (#ABC929), β–actin mAb
724 (#A1978). (3) from other vendors: HTT mAb MW8 (epitope: HD exon 1 with 67Q; Develop
725 Studies Hybridoma Bank, University of Iowa), HTT mAb PHP2 (CHDI-90001516-2,
726 Coriell/CHDI), Beclin 1 mAb (BD Biosciences, #612113), LC3 pAb (Novus Biologics, #NB100-
727 2220), p62/SQSTM1 mAb (BD Biosciences, #610832) or C-term-specific p62/SQSTM1 Guinea
728 Pig pAb (Progen Biotechnik #C-1620); ubiquitin pAb (Dako Agilent, #Z0458), ubiquitin pAb
729 (Abcam, #ab7780), LAMP1 rat mAb (Developmental Studies Hybridoma Bank, #H4A3), CTSB
730 goat pAb (Neuromics, #GT15047). (4) In-house made: CTSD pAb (RU4). CTSD sheep pAb (D-
731 2-3)(Cataldo, Thayer et al. 1990).
732 The following secondary antibodies and reagents for immunoperoxidase labeling were
733 purchased from Vector Laboratories (Burlingame, CA): biotinylated goat anti-rabbit or -mouse
734 IgG/IgM, Vectastain ABC kit (PK-4000), and DAB Peroxidase Substrate Kit (SK-4100). Mouse
735 on Mouse (M.O.M) detection kit (BMK-2201), normal-goat (S-100) and normal-donkey (S-2000-
736 20) serum blocking solution were also from Vector Lab. The following secondary antibodies for
737 immunofluorescence were purchased from Thermo Fisher Scientific (Waltham, MA): Alexa Fluor
738 488-conjugated goat anti-rabbit IgG (A11034), Alexa Fluor 568- goat anti-rabbit IgG (A11036),
739 Alexa Fluor 647- goat anti-rabbit (A21245), Alexa Fluor Plus 405- goat anti-rabbit (A48254),
740 Alexa Fluor 568- goat anti-mouse IgG (A11031), Alexa Fluor 647- goat anti-mouse (A21235) and
741 Alexa Fluor 647- goat anti-rat (A21247). HRP- linked secondary antibodies for immunoblotting
742 were obtained from Jackson ImmunoResearch Laboratories (West Grove, PA): Rabbit IgG (711-
743 035-152), Mouse IgG (711-035-150), Rat IgG (712-035-150), and Goat IgG (705-035-003).
744
745 ***Immunolabeling of brain sections:*** Immunoperoxidase and immunofluorescence IHC were
746 performed according to the protocols previously described (Yang, Lee et al. 2009, Lee, Rao et al.
747 2019). Brain vibratome sections (40 μm) were blocked and incubated in primary antibody O/N (up
748 to 3 days in some cases) at 4°C. ABC detection method was used for immunoperoxidase labeling
749 visualized with DAB while Alexa-Fluor conjugated secondary antibodies were used for
750 immunofluorescence. Autofluorescence was quenched with 1% Sudan black (Sigma-Aldrich; St.
751 Louis, MO) in 70% ethanol for 20 minutes. DAB labeled sections was inspected on a Zeiss

752 AxioSkop II equipped with a HrM digital camera (Carl Zeiss, Germany). Immunofluoescently
753 labeled sections were examined on a Zeiss LSM880 confocal microscope.
754
755 ***Confocal image collection and hue-angle based quantitative analysis for AV/LY subtypes:***
756 Confocal imaging was performed using a plan-Apochromat 20x or 40x/1.4 oil objective lens on a
757 LSM880 laser scanning confocal microscope with the following parameters: eGFP (ex: 488, em:
758 490-560 with MBS 488), mRFP (ex: 561, em: 582-640 with MBS 458/561), Alexafluor 647 (ex:
759 633, em: 640-710 with MBS 488/561/633) and DAPI (ex: 405, em: 410-483), with the 'best signal
760 scanning mode' which separates scanning tracks for each excitation and emission set to exclude
761 crosstalk between each fluorophore signal. The resolution of 40x images was 1024 x 1024 pixels
762 (corresponding to an area of 212.34 x 212.34 μm^2), and the resolution of 3x digitally zoomed
763 images was also 1024 x 1024 pixels (corresponding to an area of 70.78 x 70.78 μm^2). Detailed
764 settings for image collection were reported previously (Lee, Rao et al. 2019).
765 Hue angle-based vesicle analysis enables quantitative determination of AV/LY subtypes
766 including AP, AL, poorly acidified AL (pa-AL) and pure LY and the method was described in
767 detail previously (Lee, Rao et al. 2019). Briefly, high resolution confocal images containing the
768 LC3 (red and green) and CTSD (blue) punctate signals were analyzed with the Zen Blue Image
769 Analysis Module from Carl Zeiss Microscopy. Threshold for each of the three-color channels (red,
770 green, blue; RGB) was set by taking the average of intensity value from 20 neuronal perikarya.
771 The signal was segmented into discrete puncta by using the automatic watershed function to
772 separate clumped vesicles into individual puncta. Background signal was eliminated using the size
773 exclusion function of Zen Blue. The R, G and B intensity values of each vesicle were calculated
774 using the profile function of Zen Blue. The RGB ratio of each vesicle was converted into a hue
775 angle and saturation range – which we assigned to each AV subtype and should match the desired
776 AV color range as perceived visually (i.e., yellow for AP, blue for Ly, purple for AL and white for
777 de-acidified AL) – by entering the values of R, G, and B for a given punctum into the formula, as
778 follows: Hue° = IF(180/PI()*ATAN2(2*R-G-B,SQRT(3)*(G-B)) < 0,180/PI()*ATAN2(2*R-G-
779 B,SQRT(3) *(G-B)) + 360,180/PI()*ATAN2(2*R-G-B,SQRT(3)*(G-B))). Saturation percent of
780 the hue angle was calculated by entering the values of R, G, and B for a given punctum into the
781 following formula = (MAX(RGB)-MIN(RGB))/SUM(MAX(RGB)+MIN(RGB))*100
782 (www.workwithcolor.com), provided lightness is less than 1, which is the usual case for our data.

783 Hue angle was converted to color using the Hue color wheel. The data was pooled and categorized
784 in Excel spreadsheets.
785
786 ***Ultrastructural analyses:*** Vibratome brain sections (50 µm) were treated with 1% osmium
787 tetroxide in 100 mM sodium cacodylate buffer pH 7.4 for 30 minutes, washed in distilled water
788 four times (10 min/wash), and then treated with 2% aqueous uranyl acetate overnight at 4°C in the
789 dark. Samples were then washed and sequentially dehydrated with increasing concentrations of
790 ethanol (20, 30, 50, 70, 90, and 100%) for 30 min each, followed by three additional treatments
791 with 100% ethanol for 20 min each. Samples were then infiltrated with increasing concentrations
792 of Spurr's resin (25% for 1 h, 50% for 1 h, 75% for 1 h, 100% for 1 h, 100% overnight at room
793 temperature), and then incubated overnight at 70°C in a resin mold. For TEM ultrastructural
794 analysis, 70 nm sections were cut using a Leica Reichert Ultracut S ultramicrotome and a Diatome
795 diamond knife, placed on to grids and then post stained with 2% uranyl acetate and lead citrate.
796 Images were taken using a Ceta Camera on a ThermoFisher Talos L120C transmission electron
797 microscope operating at 120kV.
798 For post-embedding IEM, ultrathin sections were placed on to carbon formvar 75 mesh nickel
799 grids and etched using 4% sodium metaperidotate for 10 minutes before being washed twice in
800 distilled water and then blocked for one hour. Grids were incubated in the primary antibodies at 4
801 °C overnight. Next day grids underwent seven washes in 1xPBS and were then incubated in anti-
802 mouse or anti rabbit 10 nm gold secondary (1/50 dilution) for 1 hour. After this the grid was
803 washed seven times in 1xPBS and twice in distilled water. Grids were then silver enhanced for 5
804 minutes (Nanoprobes). Grids were finally post stained with 1% uranyl acetate for 5 minutes
805 followed by two washes in water and then stained with lead citrate for 5 minutes followed by a
806 final two washes in distilled water. Samples were then imaged on a ThermoFisher Talos L120C
807 operating at 120kV.
808
809 ***Western blotting****:* Samples for WB were prepared by homogenizing brains in a tissue-
810 homogenizing buffer (250 mM sucrose, 20 mM Tris pH 7.4, 1 mM EDTA, 1 mM EGTA)
811 containing protease and phosphatase inhibitors as previously described. (Schmidt, Nixon et al.
812 2012) Following electrophoresis, proteins were transferred onto 0.2 µm-pore nitrocellulose
813 membranes (Whatman, Florham Park, NJ) at 100 mA for 8-12 hours depending on the target

814 protein. The blots were blocked for 1 hour in 5% non-fat milk in TBS, rinsed in TBST (TBS +
815 0.1% Tween-20), then incubated with a primary antibody in 1% BSA/TBST overnight at 4°C. The
816 membrane was washed and incubated in a HRP conjugated goat-anti rabbit or mouse secondary
817 antibody, diluted 1:5000 in 5% milk for 1 hr at room temperature. The membrane was again
818 washed and then incubated in a Novex ECL (Invitrogen) for 1 min. The detection of the signals
819 was achieved through either exposure to a film or scanning by a digital gel imager (Syngene G:Box
820 XX9) as specified in the figure legends. Densitometry was performed with Image J and the results
821 were normalized by the immunoblot(s) of given loading control protein(s) (usually GAPDH,
822 unless otherwise noted).
823

References

Abd-Elrahman, K. S., A. Hamilton, S. R. Hutchinson, F. Liu, R. C. Russell and S. S. G. Ferguson (2017). "mGluR5 antagonism increases autophagy and prevents disease progression in the zQ175 mouse model of Huntington's disease." Sci Signal **10**(510).

Aktar, F., C. Burudpakdee, M. Polanco, S. Pei, T. C. Swayne, P. N. Lipke and L. Emtage (2019). "The huntingtin inclusion is a dynamic phase-separated compartment." Life Sci Alliance **2**(5).

Ashkenazi, A., C. F. Bento, T. Ricketts, M. Vicinanza, F. Siddiqi, M. Pavel, F. Squitieri, M. C. Hardenberg, S. Imarisio, F. M. Menzies and D. C. Rubinsztein (2017). "Polyglutamine tracts regulate beclin 1-dependent autophagy." Nature **545**(7652): 108-111.

Atwal, R. S., J. Xia, D. Pinchev, J. Taylor, R. M. Epand and R. Truant (2007). "Huntingtin has a membrane association signal that can modulate huntingtin aggregation, nuclear entry and toxicity." Hum Mol Genet **16**(21): 2600-2615.

Baiamonte, B. A., F. A. Lee, S. T. Brewer, D. Spano and G. J. LaHoste (2013). "Attenuation of Rhes activity significantly delays the appearance of behavioral symptoms in a mouse model of Huntington's disease." PLoS One **8**(1): e53606.

Barker, R. A., M. Fujimaki, P. Rogers and D. C. Rubinsztein (2020). "Huntingtin-lowering strategies for Huntington's disease." Expert Opin Investig Drugs **29**(10): 1125-1132.

Bates, G. P., R. Dorsey, J. F. Gusella, M. R. Hayden, C. Kay, B. R. Leavitt, M. Nance, C. A. Ross, R. I. Scahill, R. Wetzel, E. J. Wild and S. J. Tabrizi (2015). "Huntington disease." Nat Rev Dis Primers **1**: 15005.

Bensalem, J., C. Fourrier, L. K. Hein, S. Hassiotis, C. G. Proud and T. J. Sargeant (2021). "Inhibiting mTOR activity using AZD2014 increases autophagy in the mouse cerebral cortex." Neuropharmacology **190**: 108541.

Berg, M. J., Veeranna, C. M. Peterhoff, A. Kumar, P. S. Mohan, P. Stavrides, D. M. Marchionini, D. S. Yang and R. A. Nixon (2024). "Pathobiology of the autophagy-lysosomal pathway in the Huntington's disease brain." bioRxiv.

Bjørkøy, G., T. Lamark, A. Brech, H. Outzen, M. Perander, A. Øvervatn, H. Stenmark and T. Johansen (2005). "p62/SQSTM1 forms protein aggregates degraded by autophagy and has a protective effect on huntingtin-induced cell death." J Cell Biol **171**(4): 603-614.

Boland, B., W. H. Yu, O. Corti, B. Mollereau, A. Henriques, E. Bezard, G. M. Pastores, D. C. Rubinsztein, R. A. Nixon, M. R. Duchen, G. R. Mallucci, G. Kroemer, B. Levine, E. L. Eskelinen, F. Mochel, M. Spedding, C. Louis, O. R. Martin and M. J. Millan (2018). "Promoting the clearance of neurotoxic proteins in neurodegenerative disorders of ageing." Nat Rev Drug Discov **17**(9): 660-688.

Carty, N., N. Berson, K. Tillack, C. Thiede, D. Scholz, K. Kottig, Y. Sedaghat, C. Gabrysiak, G. Yohrling, H. von der Kammer, A. Ebneth, V. Mack, I. Munoz-Sanjuan and S. Kwak (2015). "Characterization of HTT inclusion size, location, and timing in the zQ175 mouse model of Huntington's disease: an in vivo high-content imaging study." PLoS One **10**(4): e0123527.

Cataldo, A. M., C. Y. Thayer, E. D. Bird, T. R. Wheelock and R. A. Nixon (1990). "Lysosomal proteinase antigens are prominently localized within senile plaques of Alzheimer's disease: evidence for a neuronal origin." Brain Res **513**(2): 181-192.

Cortes, C. J. and A. R. La Spada (2014). "The many faces of autophagy dysfunction in Huntington's disease: from mechanism to therapy." Drug Discov Today **19**(7): 963-971.

Croce, K. R. and A. Yamamoto (2019). "A role for autophagy in Huntington's disease." Neurobiol Dis **122**: 16-22.

Deng, Y., H. Wang, M. Joni, R. Sekhri and A. Reiner (2021). "Progression of basal ganglia pathology in heterozygous Q175 knock-in Huntington's disease mice." J Comp Neurol **529**(7): 1327-1371.

DiFiglia, M., E. Sapp, K. O. Chase, S. W. Davies, G. P. Bates, J. P. Vonsattel and N. Aronin (1997). "Aggregation of huntingtin in neuronal intranuclear inclusions and dystrophic neurites in brain." Science **277**(5334): 1990-1993.

Franklin, G. L., H. A. G. Teive, F. S. Tensini, C. H. F. Camargo, N. S. C. de Lima, D. C. de Dos Santos, A. T. Meira and S. J. Tabrizi (2024). "The Huntington's Disease Gene Discovery." Mov Disord **39**(2): 227-234.

Fu, A., V. Cohen-Kaplan, N. Avni, I. Livneh and A. Ciechanover (2021). "p62-containing, proteolytically active nuclear condensates, increase the efficiency of the ubiquitin-proteasome system." Proc Natl Acad Sci U S A **118**(33).

Gutekunst, C. A., S. H. Li, H. Yi, J. S. Mulroy, S. Kuemmerle, R. Jones, D. Rye, R. J. Ferrante, S. M. Hersch and X. J. Li (1999). "Nuclear and neuropil aggregates in Huntington's disease: relationship to neuropathology." J Neurosci **19**(7): 2522-2534.

Heikkinen, T., T. Bragge, J. Kuosmanen, T. Parkkari, S. Gustafsson, M. Kwan, J. Beltran, A. Ghavami, S. Subramaniam, N. Shahani, U. N. Ramirez-Jarquin, L. Park, I. Munoz-Sanjuan and D. M. Marchionini (2021). "Global Rhes knockout in the Q175 Huntington's disease mouse model." PLoS One **16**(10): e0258486.

Hickey, M. A., A. Kosmalska, J. Enayati, R. Cohen, S. Zeitlin, M. S. Levine and M. F. Chesselet (2008). "Extensive early motor and non-motor behavioral deficits are followed by striatal neuronal loss in knock-in Huntington's disease mice." Neuroscience **157**(1): 280-295.

Iwata, A., J. C. Christianson, M. Bucci, L. M. Ellerby, N. Nukina, L. S. Forno and R. R. Kopito (2005). "Increased susceptibility of cytoplasmic over nuclear polyglutamine aggregates to autophagic degradation." Proc Natl Acad Sci U S A **102**(37): 13135-13140.

Iwata, A., Y. Nagashima, L. Matsumoto, T. Suzuki, T. Yamanaka, H. Date, K. Deoka, N. Nukina and S. Tsuji (2009). "Intranuclear degradation of polyglutamine aggregates by the ubiquitin-proteasome system." J Biol Chem **284**(15): 9796-9803.

Jamilloux, Y., B. Lagrange, A. Di Micco, E. Bourdonnay, A. Provost, R. Tallant, T. Henry and F. Martinon (2018). "A proximity-dependent biotinylation (BioID) approach flags the p62/sequestosome-1 protein as a caspase-1 substrate." J Biol Chem **293**(32): 12563-12575.

Jiang, A., R. R. Handley, K. Lehnert and R. G. Snell (2023). "From Pathogenesis to Therapeutics: A Review of 150 Years of Huntington's Disease Research." Int J Mol Sci **24**(16).

Jiang, Y., J. J. Alam, S. N. Gomperts, P. Maruff, A. W. Lemstra, U. A. Germann, P. H. Stavrides, S. Darji, S. Malampati, J. Peddy, C. Bleiwas, M. Pawlik, A. Pensalfini, D. S. Yang, S. Subbanna, B. S. Basavarajappa, J. F. Smiley, A. Gardner, K. Blackburn, H. M. Chu, N. D. Prins, C. E. Teunissen, J. E. Harrison, P. Scheltens and R. A. Nixon (2022). "Preclinical and randomized clinical evaluation of the p38alpha kinase inhibitor neflamapimod for basal forebrain cholinergic degeneration." Nat Commun **13**(1): 5308.

Kim, A., K. Lalonde, A. Truesdell, P. Gomes Welter, P. S. Brocardo, T. R. Rosenstock and J. Gil-Mohapel (2021). "New Avenues for the Treatment of Huntington's Disease." Int J Mol Sci **22**(16).

Kim, Y. C. and K. L. Guan (2015). "mTOR: a pharmacologic target for autophagy regulation." J Clin Invest **125**(1): 25-32.

Kim, Y. J., Y. Yi, E. Sapp, Y. Wang, B. Cuiffo, K. B. Kegel, Z. H. Qin, N. Aronin and M. DiFiglia (2001). "Caspase 3-cleaved N-terminal fragments of wild-type and mutant huntingtin are present in normal and Huntington's disease brains, associate with membranes, and undergo calpain-dependent proteolysis." Proc Natl Acad Sci U S A **98**(22): 12784-12789.

Klionsky, D. J., G. Petroni, R. K. Amaravadi, E. H. Baehrecke, A. Ballabio, P. Boya, J. M. Bravo-San Pedro, K. Cadwell, F. Cecconi, A. M. K. Choi, M. E. Choi, C. T. Chu, P. Codogno, M. I. Colombo, A. M. Cuervo, V. Deretic, I. Dikic, Z. Elazar, E. L. Eskelinen, G. M. Fimia, D. A. Gewirtz, D. R. Green, M. Hansen, M.

Jaattela, T. Johansen, G. Juhasz, V. Karantza, C. Kraft, G. Kroemer, N. T. Ktistakis, S. Kumar, C. Lopez-Otin, K. F. Macleod, F. Madeo, J. Martinez, A. Melendez, N. Mizushima, C. Munz, J. M. Penninger, R. M. Perera, M. Piacentini, F. Reggiori, D. C. Rubinsztein, K. M. Ryan, J. Sadoshima, L. Santambrogio, L. Scorrano, H. U. Simon, A. K. Simon, A. Simonsen, A. Stolz, N. Tavernarakis, S. A. Tooze, T. Yoshimori, J. Yuan, Z. Yue, Q. Zhong, L. Galluzzi and F. Pietrocola (2021). "Autophagy in major human diseases." EMBO J **40**(19): e108863.

Ko, J., J. M. Isas, A. Sabbaugh, J. H. Yoo, N. K. Pandey, A. Chongtham, M. Ladinsky, W. L. Wu, H. Rohweder, A. Weiss, D. Macdonald, I. Munoz-Sanjuan, R. Langen, P. H. Patterson and A. Khoshnan (2018). "Identification of distinct conformations associated with monomers and fibril assemblies of mutant huntingtin." Hum Mol Genet **27**(13): 2330-2343.

Kolla, R., P. Gopinath, J. Ricci, A. Reif, I. Rostami and H. A. Lashuel (2021). "A New Chemoenzymatic Semisynthetic Approach Provides Insight into the Role of Phosphorylation beyond Exon1 of Huntingtin and Reveals N-Terminal Fragment Length-Dependent Distinct Mechanisms of Aggregation." J Am Chem Soc **143**(26): 9798-9812.

Lee, J. H., M. V. Rao, D. S. Yang, P. Stavrides, E. Im, A. Pensalfini, C. Huo, P. Sarkar, T. Yoshimori and R. A. Nixon (2019). "Transgenic expression of a ratiometric autophagy probe specifically in neurons enables the interrogation of brain autophagy in vivo." Autophagy **15**(3): 543-557.

Lee, J. H., L. Tecedor, Y. H. Chen, A. M. Monteys, M. J. Sowada, L. M. Thompson and B. L. Davidson (2015). "Reinstating aberrant mTORC1 activity in Huntington's disease mice improves disease phenotypes." Neuron **85**(2): 303-315.

Lee, J. H., D. S. Yang, C. N. Goulbourne, E. Im, P. Stavrides, A. Pensalfini, H. Chan, C. Bouchet-Marquis, C. Bleiwas, M. J. Berg, C. Huo, J. Peddy, M. Pawlik, E. Levy, M. Rao, M. Staufenbiel and R. A. Nixon (2022). "Faulty autolysosome acidification in Alzheimer's disease mouse models induces autophagic build-up of Abeta in neurons, yielding senile plaques." Nat Neurosci **25**(6): 688-701.

Li, H., S. H. Li, A. L. Cheng, L. Mangiarini, G. P. Bates and X. J. Li (1999). "Ultrastructural localization and progressive formation of neuropil aggregates in Huntington's disease transgenic mice." Hum Mol Genet **8**(7): 1227-1236.

Lie, P. P. Y., D. S. Yang, P. Stavrides, C. N. Goulbourne, P. Zheng, P. S. Mohan, A. M. Cataldo and R. A. Nixon (2021). "Post-Golgi carriers, not lysosomes, confer lysosomal properties to pre-degradative organelles in normal and dystrophic axons." Cell Rep **35**(4): 109034.

Lie, P. P. Y., L. Yoo, C. N. Goulbourne, M. J. Berg, P. Stavrides, C. Huo, J. H. Lee and R. A. Nixon (2022). "Axonal transport of late endosomes and amphisomes is selectively modulated by local Ca(2+) efflux and disrupted by PSEN1 loss of function." Sci Adv **8**(17): eabj5716.

Liu, K. Y., Y. C. Shyu, B. A. Barbaro, Y. T. Lin, Y. Chern, L. M. Thompson, C. K. James Shen and J. L. Marsh (2015). "Disruption of the nuclear membrane by perinuclear inclusions of mutant huntingtin causes cell-cycle re-entry and striatal cell death in mouse and cell models of Huntington's disease." Hum Mol Genet **24**(6): 1602-1616.

Marchionini, D. M., J. P. Liu, A. Ambesi-Impiombato, K. Kerker, K. Cirillo, M. Bansal, R. Mushlin, D. Brunner, S. Ramboz, M. Kwan, K. Kuhlbrodt, K. Tillack, F. Peters, L. Rauhala, J. Obenauer, J. R. Greene, C. Hartl, V. Khetarpal, B. Lager, J. Rosinski, J. Aaronson, M. Alam, E. Signer, I. Munoz-Sanjuan, D. Howland and S. O. Zeitlin (2022). "Benefits of global mutant huntingtin lowering diminish over time in a Huntington's disease mouse model." JCI Insight **7**(20).

Mario Isas, J., N. K. Pandey, H. Xu, K. Teranishi, A. K. Okada, E. K. Fultz, A. Rawat, A. Applebaum, F. Meier, J. Chen, R. Langen and A. B. Siemer (2021). "Huntingtin fibrils with different toxicity, structure, and seeding potential can be interconverted." Nat Commun **12**(1): 4272.

Martin, D. D., S. Ladha, D. E. Ehrnhoefer and M. R. Hayden (2015). "Autophagy in Huntington disease and huntingtin in autophagy." Trends Neurosci **38**(1): 26-35.

964 Martinez-Vicente, M., Z. Talloczy, E. Wong, G. Tang, H. Koga, S. Kaushik, R. de Vries, E. Arias, S. Harris, D.
965 Sulzer and A. M. Cuervo (2010). "Cargo recognition failure is responsible for inefficient autophagy
966 in Huntington's disease." Nat Neurosci **13**(5): 567-576.
967 Menalled, L. B., A. E. Kudwa, S. Miller, J. Fitzpatrick, J. Watson-Johnson, N. Keating, M. Ruiz, R. Mushlin,
968 W. Alosio, K. McConnell, D. Connor, C. Murphy, S. Oakeshott, M. Kwan, J. Beltran, A. Ghavami, D.
969 Brunner, L. C. Park, S. Ramboz and D. Howland (2012). "Comprehensive behavioral and molecular
970 characterization of a new knock-in mouse model of Huntington's disease: zQ175." PLoS One **7**(12):
971 e49838.
972 Menalled, L. B., J. D. Sison, I. Dragatsis, S. Zeitlin and M. F. Chesselet (2003). "Time course of early motor
973 and neuropathological anomalies in a knock-in mouse model of Huntington's disease with 140
974 CAG repeats." J Comp Neurol **465**(1): 11-26.
975 Mende-Mueller, L. M., T. Toneff, S. R. Hwang, M. F. Chesselet and V. Y. Hook (2001). "Tissue-specific
976 proteolysis of Huntingtin (htt) in human brain: evidence of enhanced levels of N- and C-terminal
977 htt fragments in Huntington's disease striatum." J Neurosci **21**(6): 1830-1837.
978 Nixon, R. A. (2013). "The role of autophagy in neurodegenerative disease." Nat Med **19**(8): 983-997.
979 Norman, J. M., G. M. Cohen and E. T. Bampton (2010). "The in vitro cleavage of the hAtg proteins by cell
980 death proteases." Autophagy **6**(8): 1042-1056.
981 Ochaba, J., T. Lukacsovich, G. Csikos, S. Zheng, J. Margulis, L. Salazar, K. Mao, A. L. Lau, S. Y. Yeung, S.
982 Humbert, F. Saudou, D. J. Klionsky, S. Finkbeiner, S. O. Zeitlin, J. L. Marsh, D. E. Housman, L. M.
983 Thompson and J. S. Steffan (2014). "Potential function for the Huntingtin protein as a scaffold for
984 selective autophagy." Proc Natl Acad Sci U S A **111**(47): 16889-16894.
985 Ouimet, C. C., K. C. Langley-Gullion and P. Greengard (1998). "Quantitative immunocytochemistry of
986 DARPP-32-expressing neurons in the rat caudatoputamen." Brain Res **808**(1): 8-12.
987 Park, J. M., C. H. Jung, M. Seo, N. M. Otto, D. Grunwald, K. H. Kim, B. Moriarity, Y. M. Kim, C. Starker, R. S.
988 Nho, D. Voytas and D. H. Kim (2016). "The ULK1 complex mediates MTORC1 signaling to the
989 autophagy initiation machinery via binding and phosphorylating ATG14." Autophagy **12**(3): 547-
990 564.
991 Peng, Q., B. Wu, M. Jiang, J. Jin, Z. Hou, J. Zheng, J. Zhang and W. Duan (2016). "Characterization of
992 Behavioral, Neuropathological, Brain Metabolic and Key Molecular Changes in zQ175 Knock-In
993 Mouse Model of Huntington's Disease." PLoS One **11**(2): e0148839.
994 Peskett, T. R., F. Rau, J. O'Driscoll, R. Patani, A. R. Lowe and H. R. Saibil (2018). "A Liquid to Solid Phase
995 Transition Underlying Pathological Huntingtin Exon1 Aggregation." Mol Cell **70**(4): 588-601.e586.
996 Pressl, C., K. Mätlik, L. Kus, P. Darnell, J. D. Luo, M. R. Paul, A. R. Weiss, W. Liguore, T. S. Carroll, D. A. Davis,
997 J. McBride and N. Heintz (2024). "Selective vulnerability of layer 5a corticostriatal neurons in
998 Huntington's disease." Neuron.
999 Pryor, W. M., M. Biagioli, N. Shahani, S. Swarnkar, W. C. Huang, D. T. Page, M. E. MacDonald and S.
1000 Subramaniam (2014). "Huntingtin promotes mTORC1 signaling in the pathogenesis of
1001 Huntington's disease." Sci Signal **7**(349): ra103.
1002 Ravikumar, B., C. Vacher, Z. Berger, J. E. Davies, S. Luo, L. G. Oroz, F. Scaravilli, D. F. Easton, R. Duden, C. J.
1003 O'Kane and D. C. Rubinsztein (2004). "Inhibition of mTOR induces autophagy and reduces toxicity
1004 of polyglutamine expansions in fly and mouse models of Huntington disease." Nat Genet **36**(6):
1005 585-595.
1006 Riguet, N., A. L. Mahul-Mellier, N. Maharjan, J. Burtscher, M. Croisier, G. Knott, J. Hastings, A. Patin, V.
1007 Reiterer, H. Farhan, S. Nasarov and H. A. Lashuel (2021). "Nuclear and cytoplasmic huntingtin
1008 inclusions exhibit distinct biochemical composition, interactome and ultrastructural properties."
1009 Nat Commun **12**(1): 6579.

1010 Rose, C., F. M. Menzies, M. Renna, A. Acevedo-Arozena, S. Corrochano, O. Sadiq, S. D. Brown and D. C.
1011 Rubinsztein (2010). "Rilmenidine attenuates toxicity of polyglutamine expansions in a mouse
1012 model of Huntington's disease." Hum Mol Genet **19**(11): 2144-2153.
1013 Rothe, T., M. Deliano, A. M. Wojtowicz, A. Dvorzhak, D. Harnack, S. Paul, T. Vagner, I. Melnick, H. Stark
1014 and R. Grantyn (2015). "Pathological gamma oscillations, impaired dopamine release, synapse loss
1015 and reduced dynamic range of unitary glutamatergic synaptic transmission in the striatum of
1016 hypokinetic Q175 Huntington mice." Neuroscience **311**: 519-538.
1017 Rui, Y. N., Z. Xu, B. Patel, Z. Chen, D. Chen, A. Tito, G. David, Y. Sun, E. F. Stimming, H. J. Bellen, A. M.
1018 Cuervo and S. Zhang (2015). "Huntingtin functions as a scaffold for selective macroautophagy."
1019 Nat Cell Biol **17**(3): 262-275.
1020 Sanchez-Garrido, J., V. Sancho-Shimizu and A. R. Shenoy (2018). "Regulated proteolysis of p62/SQSTM1
1021 enables differential control of autophagy and nutrient sensing." Sci Signal **11**(559).
1022 Sarkar, S. and D. C. Rubinsztein (2008). "Huntington's disease: degradation of mutant huntingtin by
1023 autophagy." FEBS J **275**(17): 4263-4270.
1024 Sarkar, S. and D. C. Rubinsztein (2008). "Small molecule enhancers of autophagy for neurodegenerative
1025 diseases." Mol Biosyst **4**(9): 895-901.
1026 Schmidt, S. D., R. A. Nixon and P. M. Mathews (2012). "Tissue processing prior to analysis of Alzheimer's
1027 disease associated proteins and metabolites, including Abeta." Methods Mol Biol **849**: 493-506.
1028 Sotrel, A., P. A. Paskevich, D. K. Kiely, E. D. Bird, R. S. Williams and R. H. Myers (1991). "Morphometric
1029 analysis of the prefrontal cortex in Huntington's disease." Neurology **41**(7): 1117-1123.
1030 Tanaka, M., Y. Machida, S. Niu, T. Ikeda, N. R. Jana, H. Doi, M. Kurosawa, M. Nekooki and N. Nukina (2004).
1031 "Trehalose alleviates polyglutamine-mediated pathology in a mouse model of Huntington
1032 disease." Nat Med **10**(2): 148-154.
1033 The-Huntington's-Disease-Collaborative-Research-Group (1993). "A novel gene containing a trinucleotide
1034 repeat that is expanded and unstable on Huntington's disease chromosomes. ." Cell **72**(6): 971-
1035 983.
1036 Trottier, Y., Y. Lutz, G. Stevanin, G. Imbert, D. Devys, G. Cancel, F. Saudou, C. Weber, G. David, L. Tora and
1037 et al. (1995). "Polyglutamine expansion as a pathological epitope in Huntington's disease and four
1038 dominant cerebellar ataxias." Nature **378**(6555): 403-406.
1039 Valionyte, E., Y. Yang, S. A. Griffiths, A. T. Bone, E. R. Barrow, V. Sharma, B. Lu and S. Luo (2022). "The
1040 caspase-6-p62 axis modulates p62 droplets based autophagy in a dominant-negative manner."
1041 Cell Death Differ **29**(6): 1211-1227.
1042 Vodicka, P., J. Lim, D. T. Williams, K. B. Kegel, K. Chase, H. Park, D. Marchionini, S. Wilkinson, T. Mead, H.
1043 Birch, D. Yates, K. Lyons, C. Dominguez, M. Beconi, Z. Yue, N. Aronin and M. DiFiglia (2014).
1044 "Assessment of chloroquine treatment for modulating autophagy flux in brain of WT and HD
1045 mice." J Huntingtons Dis **3**(2): 159-174.
1046 Vonsattel, J. P. (2008). "Huntington disease models and human neuropathology: similarities and
1047 differences." Acta Neuropathol **115**(1): 55-69.
1048 Vonsattel, J. P., R. H. Myers, T. J. Stevens, R. J. Ferrante, E. D. Bird and E. P. Richardson, Jr. (1985).
1049 "Neuropathological classification of Huntington's disease." J Neuropathol Exp Neurol **44**(6): 559-
1050 577.
1051 Wold, M. S., J. Lim, V. Lachance, Z. Deng and Z. Yue (2016). "ULK1-mediated phosphorylation of ATG14
1052 promotes autophagy and is impaired in Huntington's disease models." Mol Neurodegener **11**(1):
1053 76.
1054 Xia, J., D. H. Lee, J. Taylor, M. Vandelft and R. Truant (2003). "Huntingtin contains a highly conserved
1055 nuclear export signal." Hum Mol Genet **12**(12): 1393-1403.

1056 Yang, D. S., J. H. Lee and R. A. Nixon (2009). "Monitoring autophagy in Alzheimer's disease and related
1057 neurodegenerative diseases." Methods Enzymol **453**: 111-144.
1058 Yang, J. and C. Zhang (2023). "Targeting the autophagy-lysosomal pathway in Huntington disease: a
1059 pharmacological perspective." Front Aging Neurosci **15**: 1175598.
1060 Zhou, Y., T. R. Peskett, C. Landles, J. B. Warner, K. Sathasivam, E. J. Smith, S. Chen, R. Wetzel, H. A. Lashuel,
1061 G. P. Bates and H. R. Saibil (2021). "Correlative light and electron microscopy suggests that mutant
1062 huntingtin dysregulates the endolysosomal pathway in presymptomatic Huntington's disease."
1063 Acta Neuropathol Commun **9**(1): 70.
1064

Fig. 1. Identification of inclusions and HTT molecular species in Q175 mice.

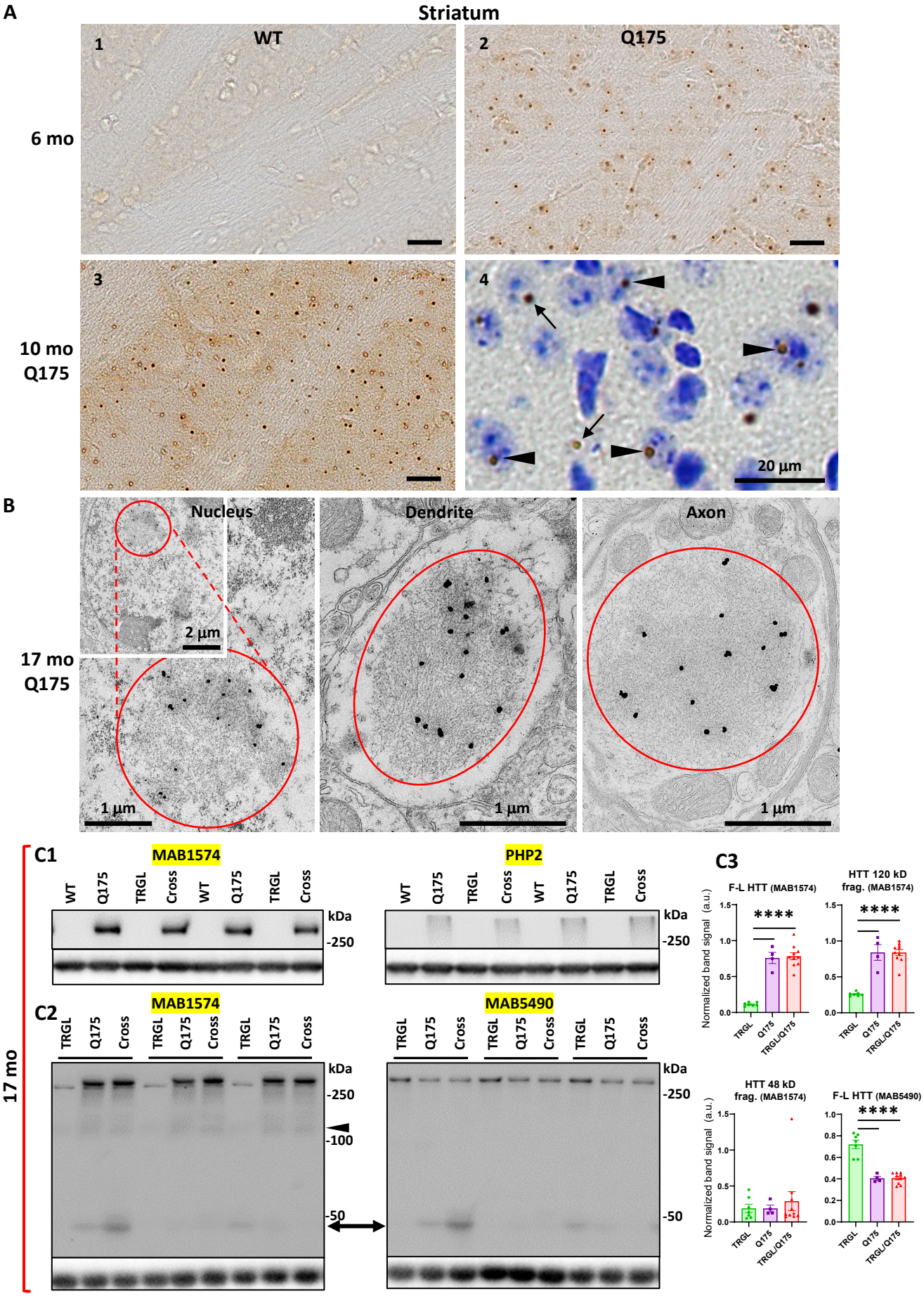

Fig. 2. HTT colocalizes with p62, Ub and CTSD

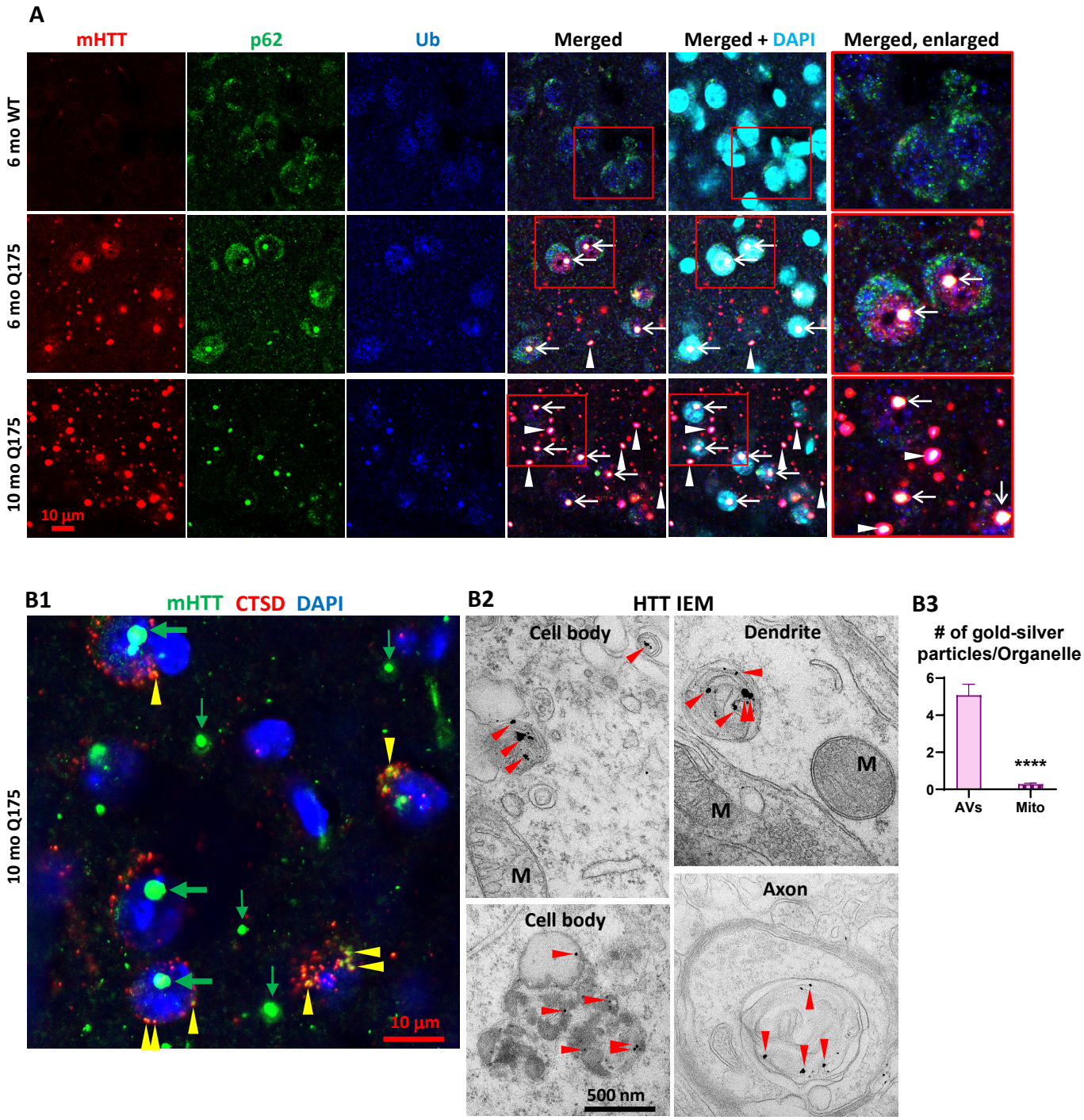

Fig. 3. Mild late-onset alterations in the ALP in the striatum of 17-mo-old Q175.

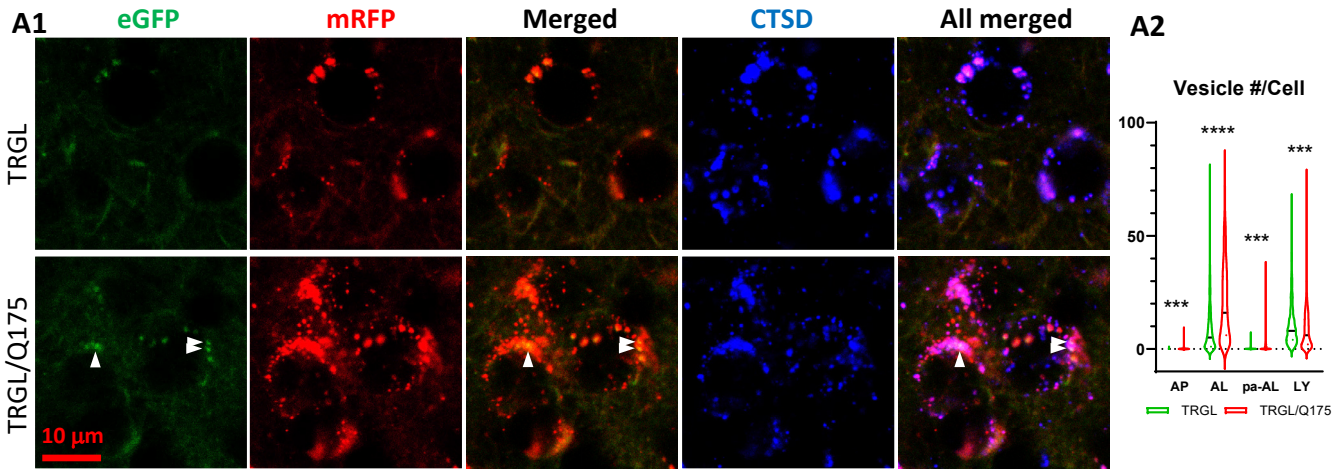

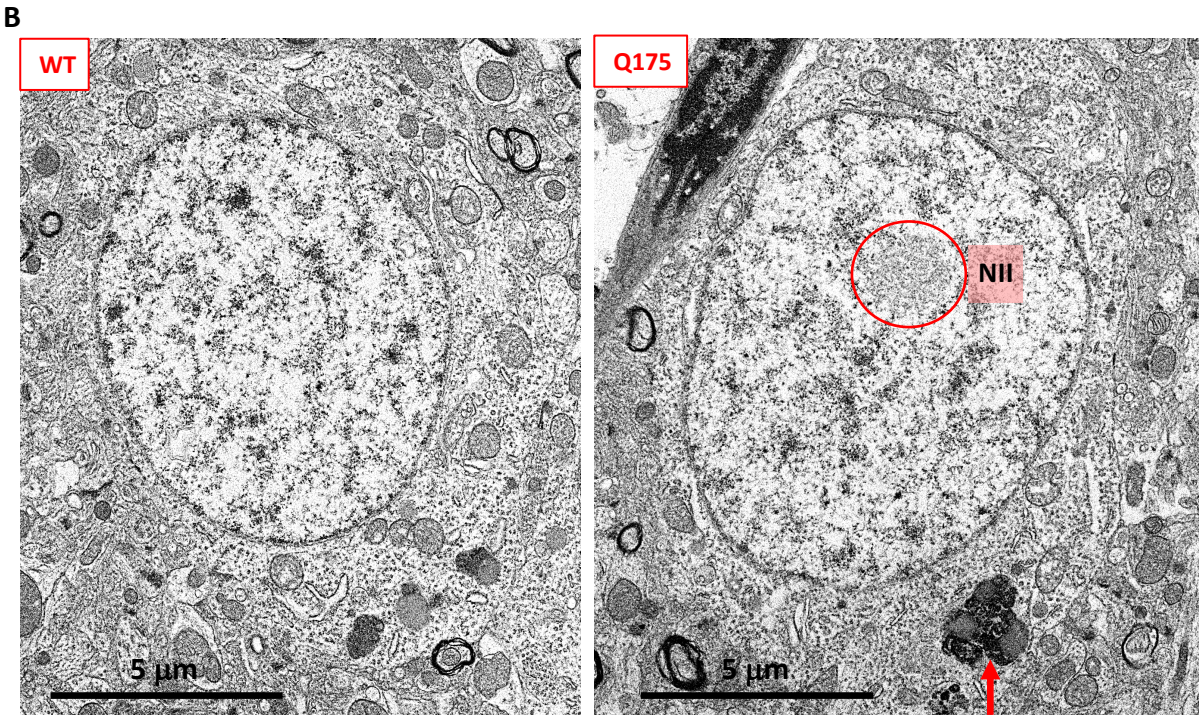

Fig. 4. DARPP-32-IR decreases in striatal neurons of 17-mo-old TRGL/Q175 in the absence of a NeuN signal reduction.

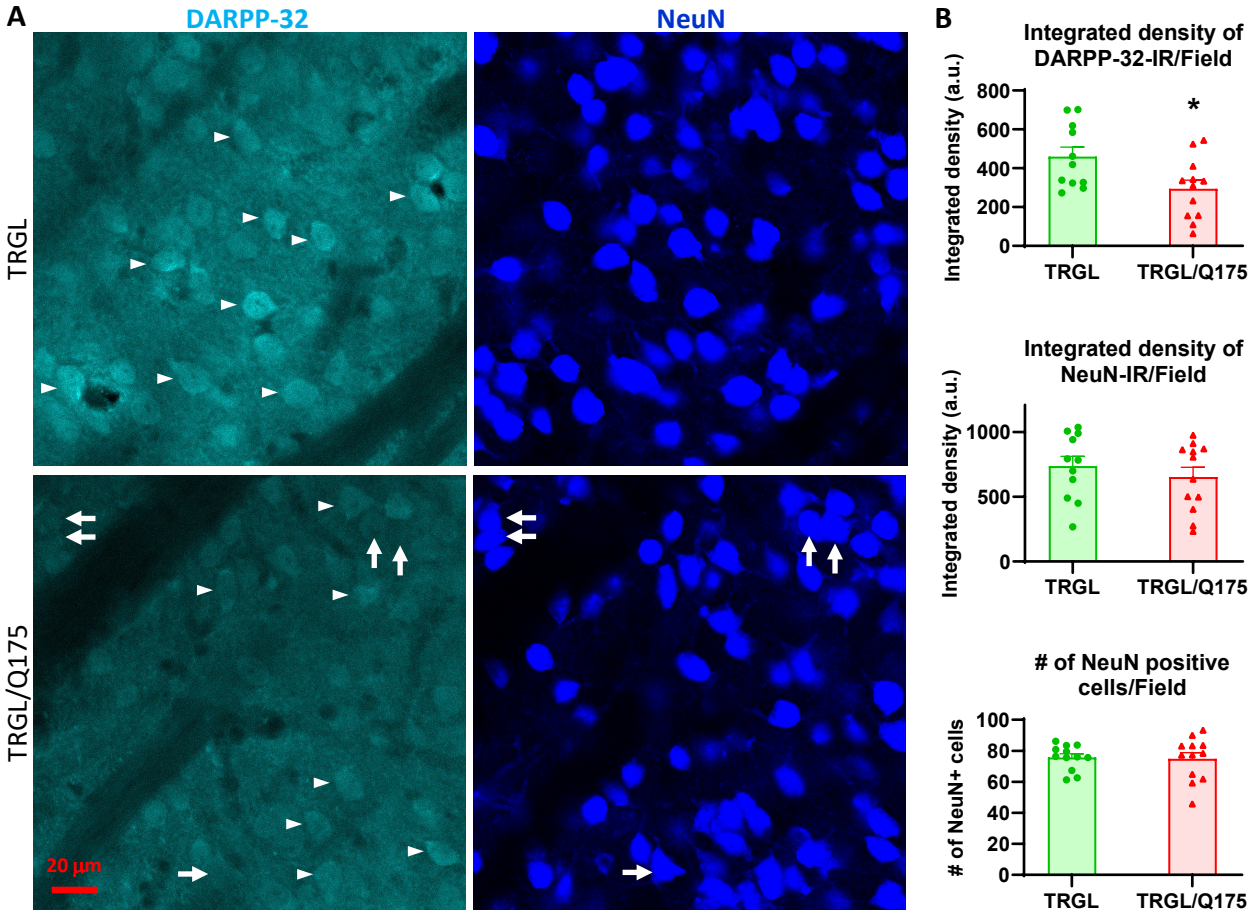

Fig. 5. mTORi INK exhibits target engagement and induces downstream responses in the ALP in 7-mo-old TRGL/Q175.

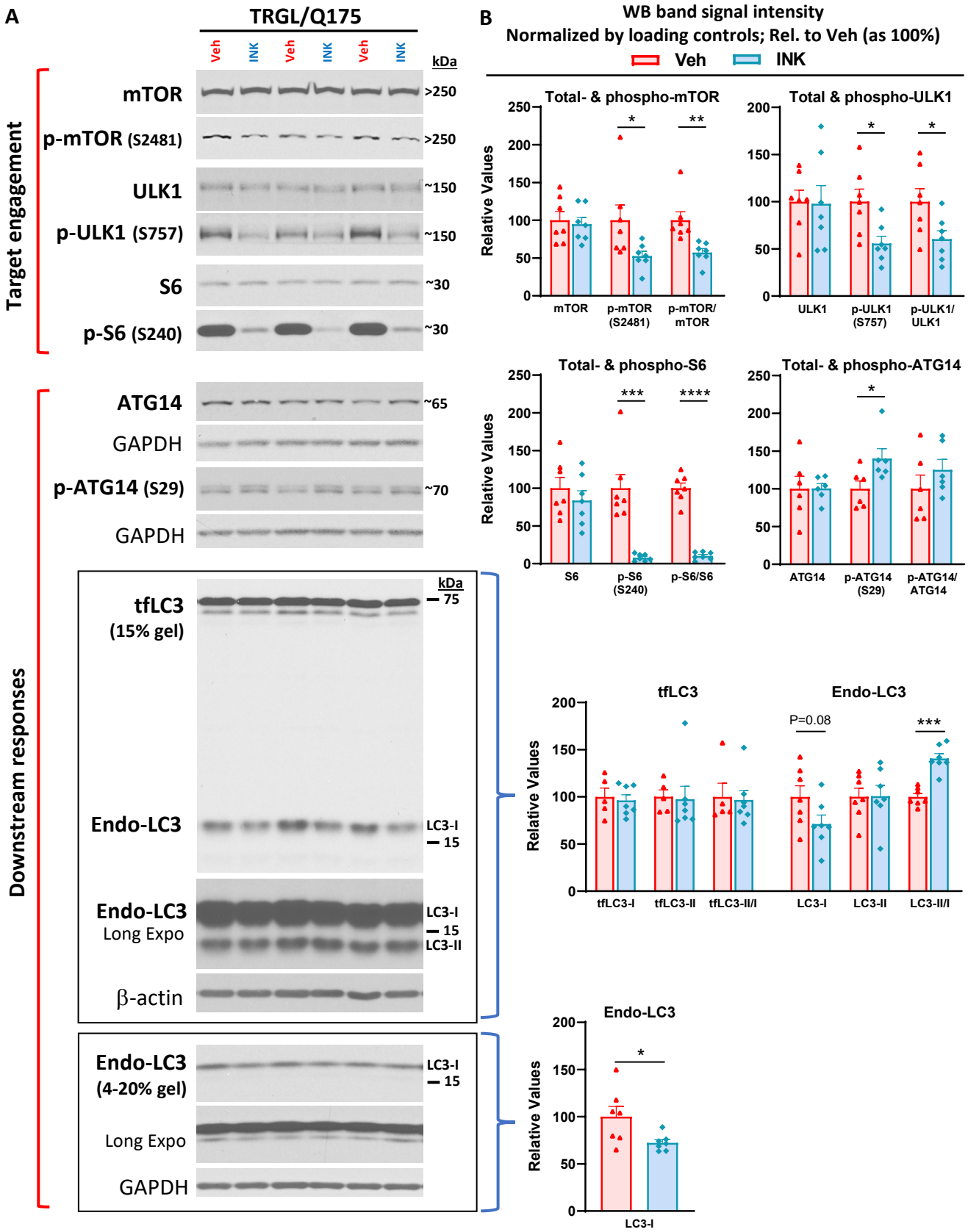

Fig. 6. mTORi INK reverses the mild alteration of AV/LY subtypes in the striatum of 7-mo-old TRGL/Q175.

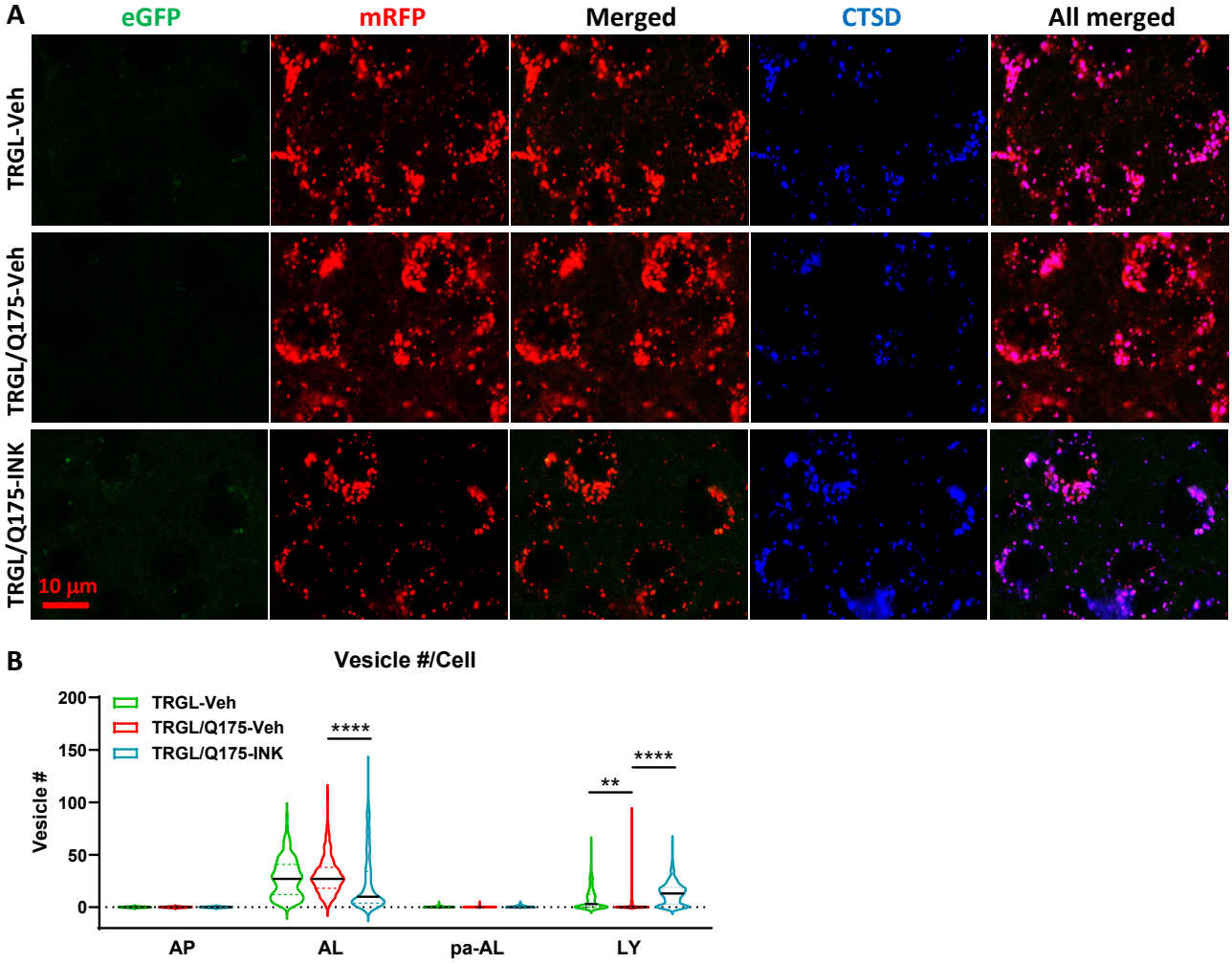

Fig. 7. mTORi INK reduces HTT-, Ub- or p62-IR-covered areas parallelly in the striatum of 7-mo-old TRGL/Q175.

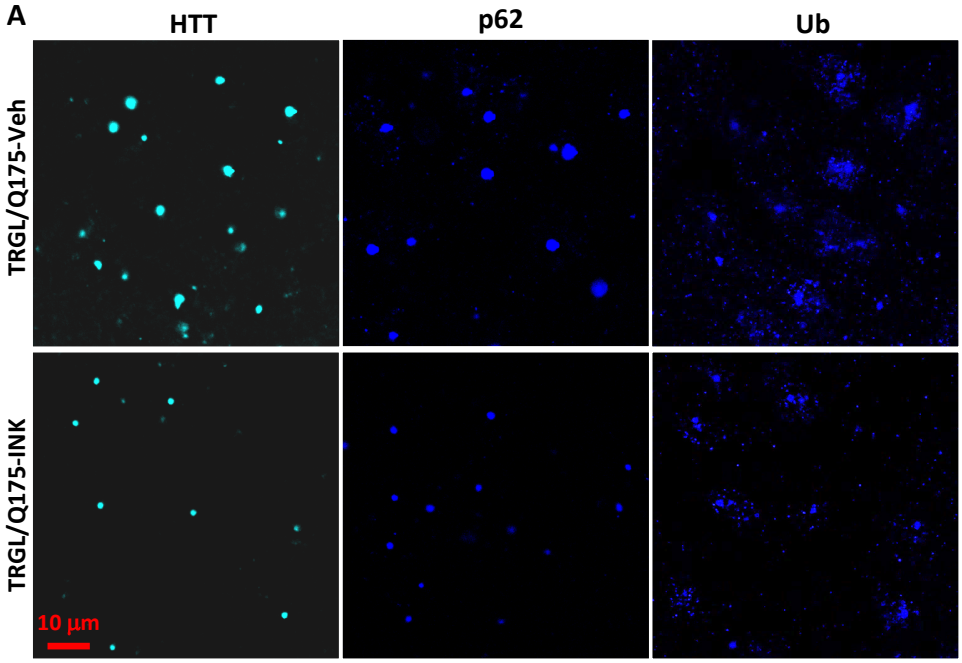

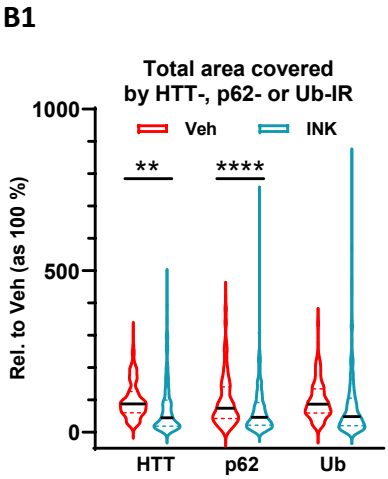

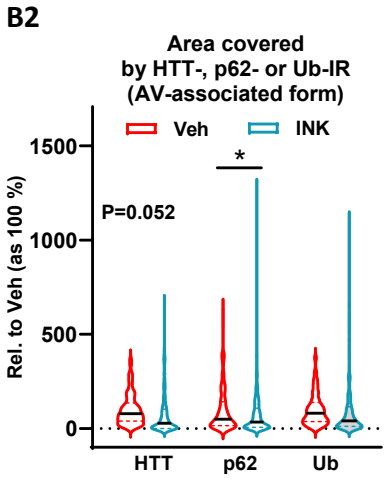

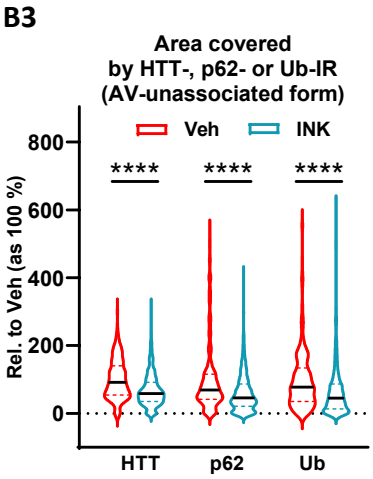

Fig. 8. INK treatment does not reverse the reduction of DARPP-32-IR in the striatum of 7-mo-old TRGL/Q175.

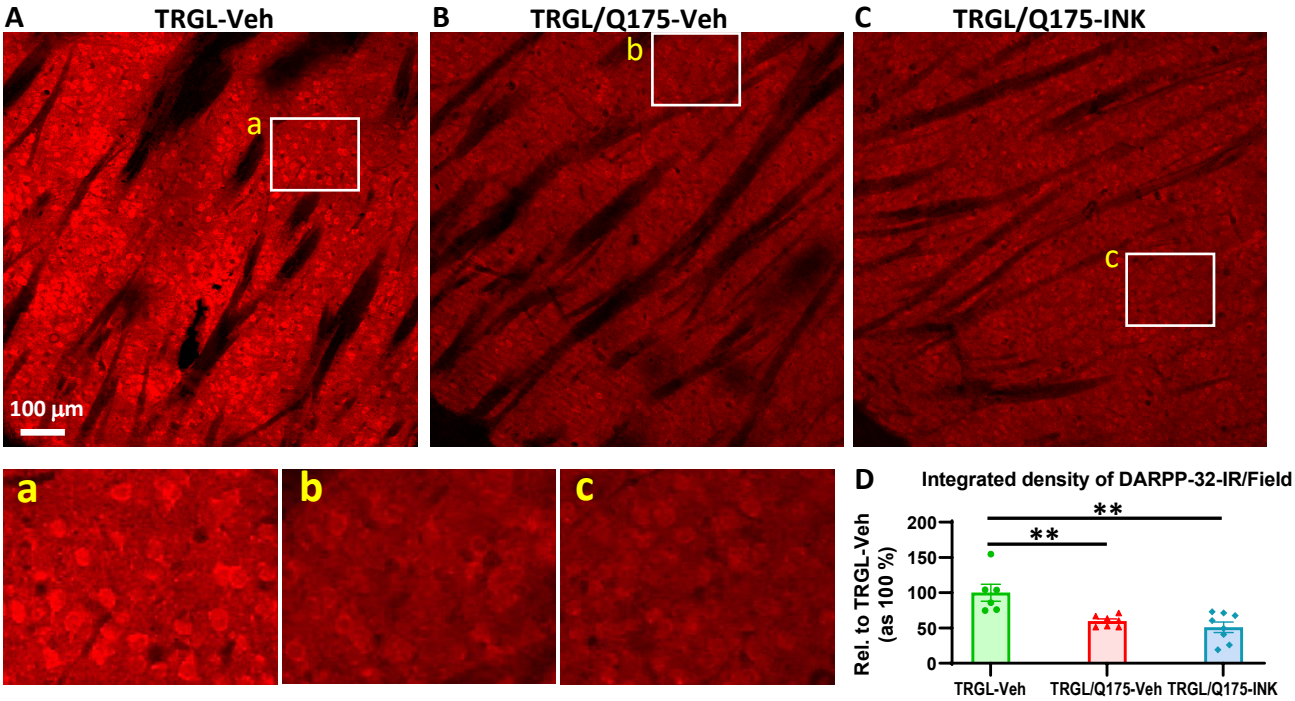

Fig. S1. Colocalization of HTT/Ub and Ub/p62 in IBs in the STR.

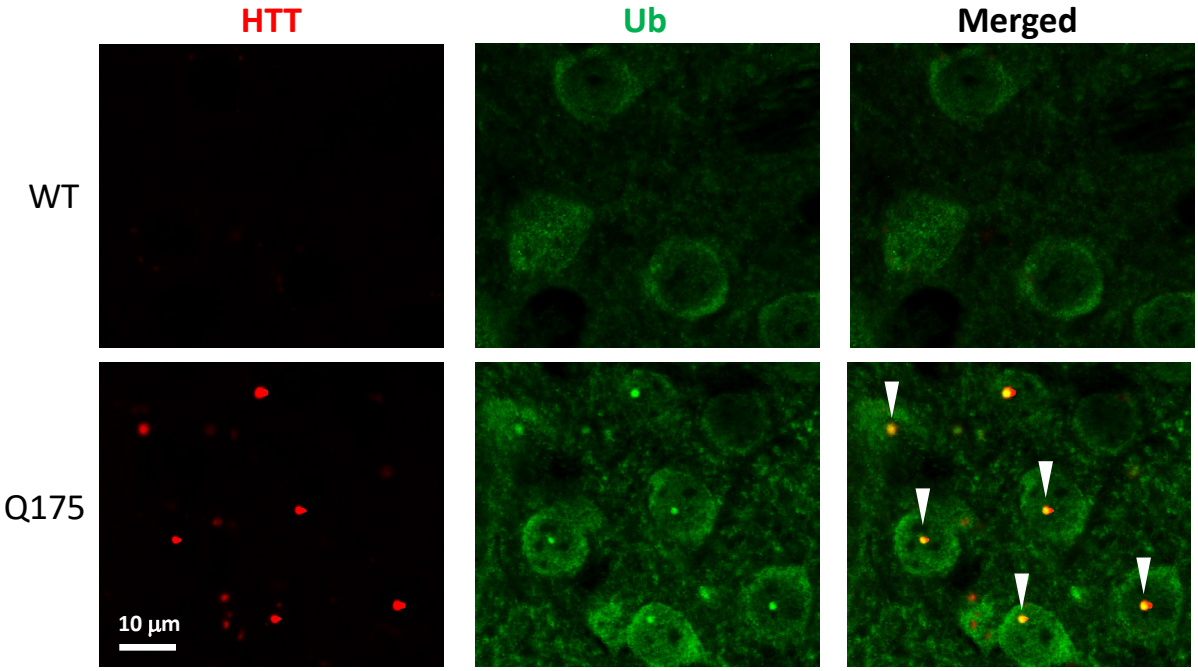

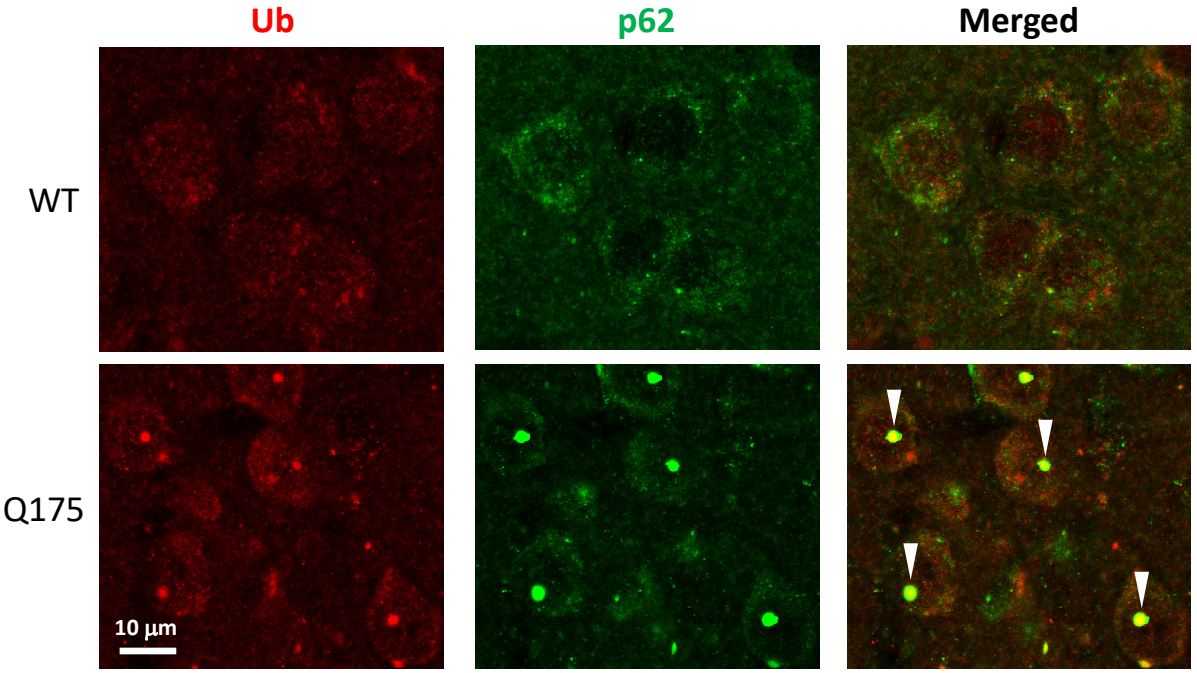

Fig. S2 (related to Fig. 3). Molecules involved in various stages of the ALP are largely unchanged in 17-mo-old TRGL/Q175.

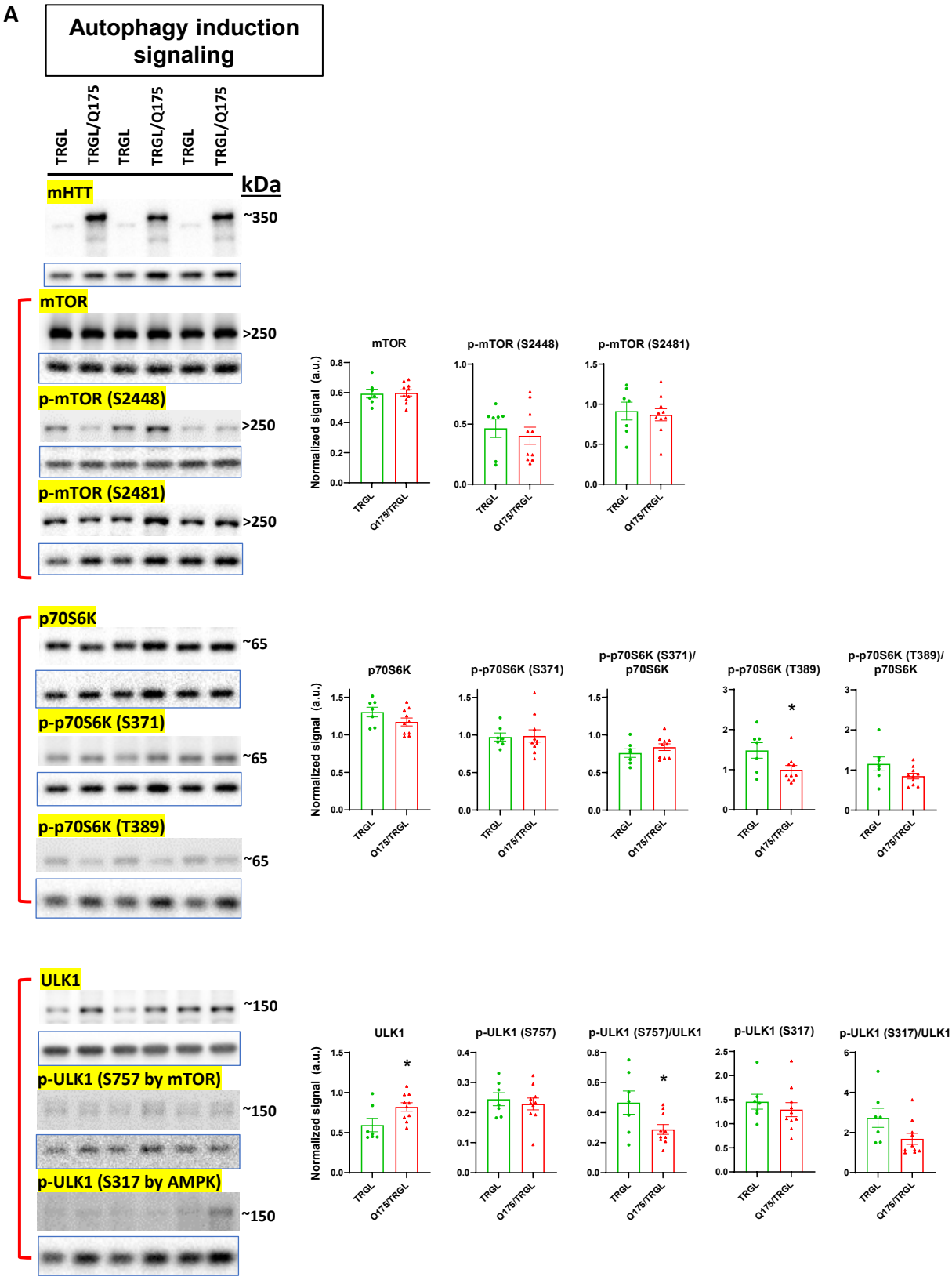

Fig. S2 (related Fig. 3). Molecules involved in various stages of the ALP are largely unchanged in 17-mo-old TRGL/Q175. (Cont'd)

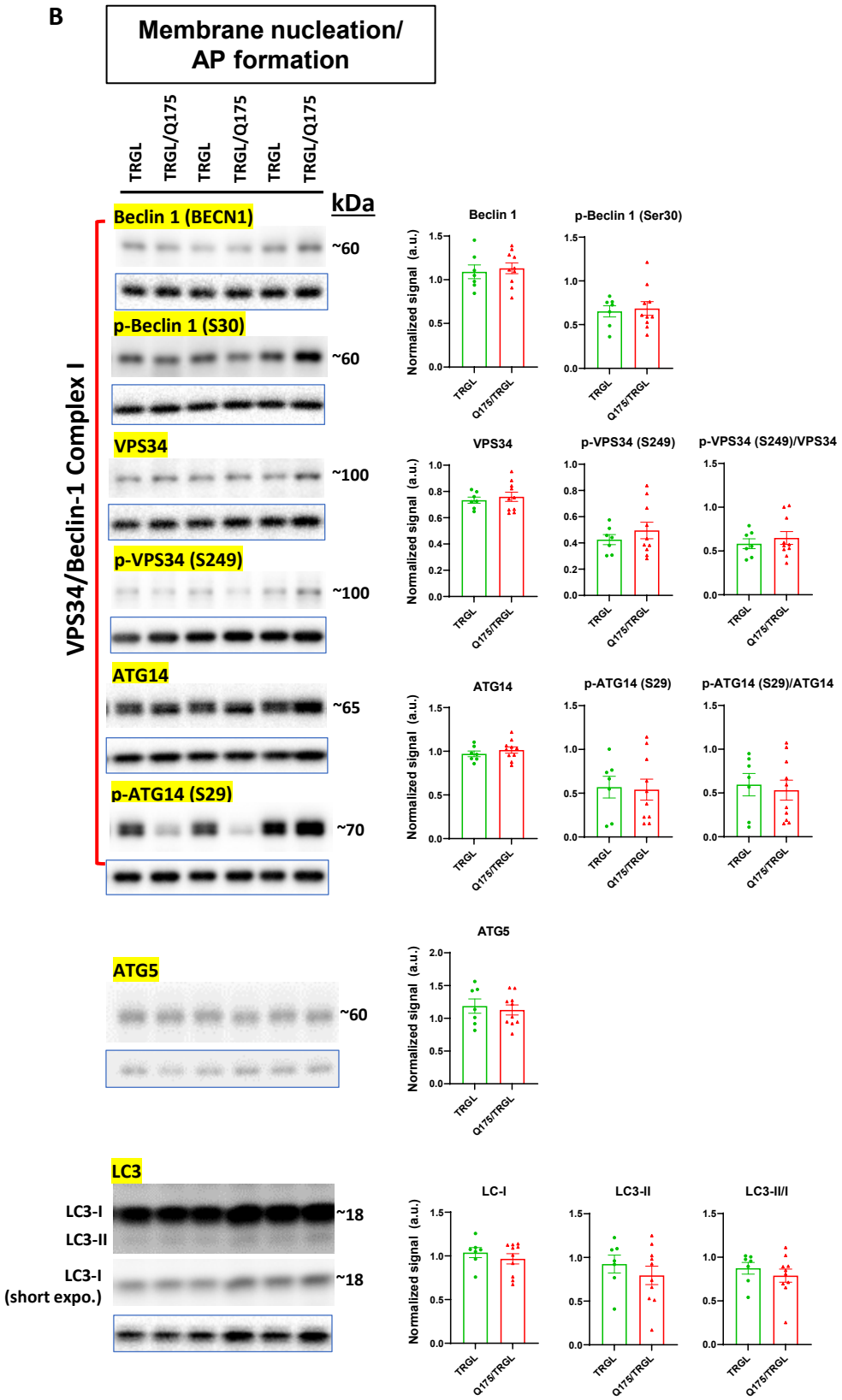

Fig. S2 (related to Fig. 3). Molecules involved in various stages of the ALP are largely unchanged in 17-mo-old TRGL/Q175. (Cont'd)

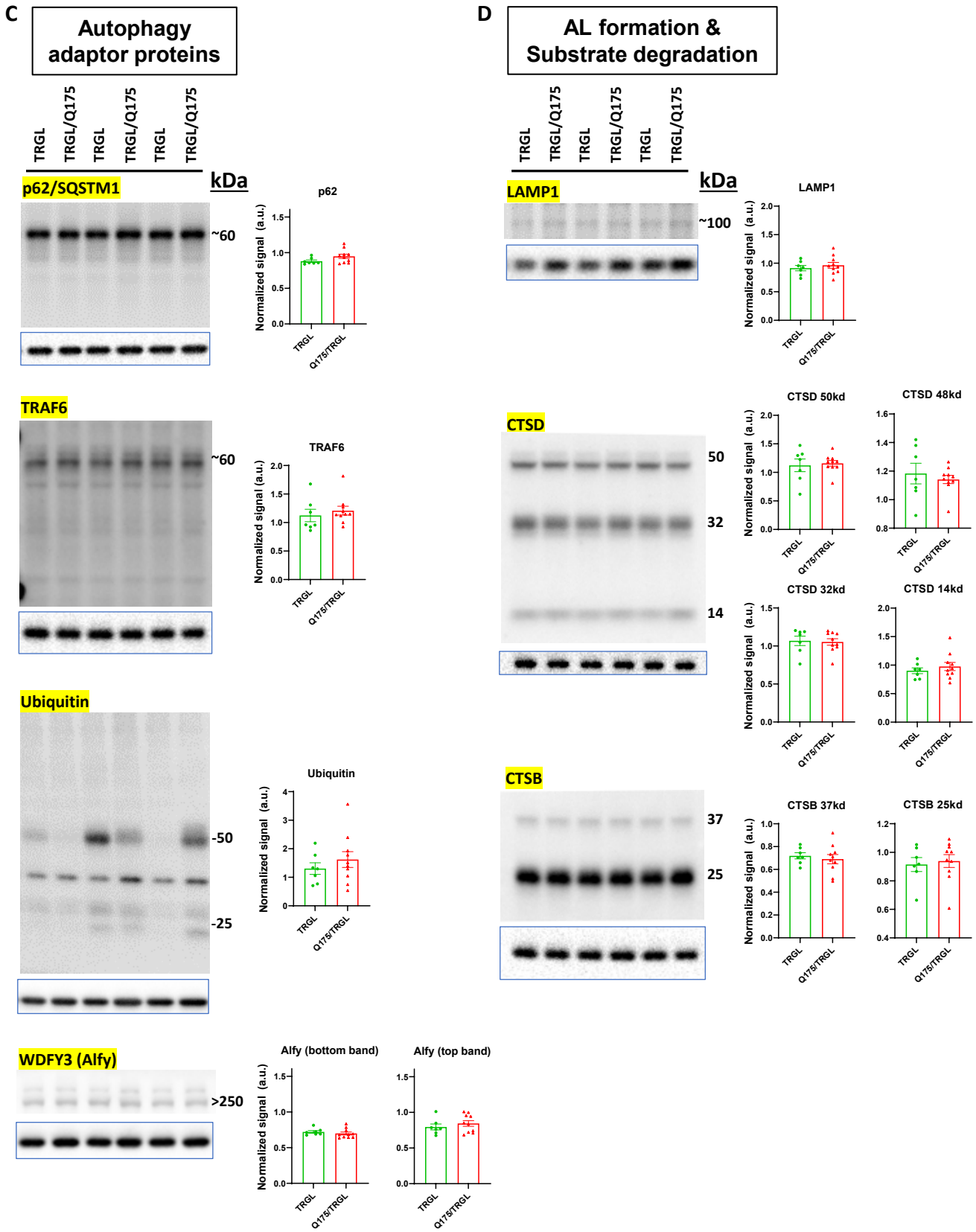

Fig. S3 (related to Fig. 5). Dosing tests demonstrate mTORi INK BBB penetration and target engagement even at low dosages.

A

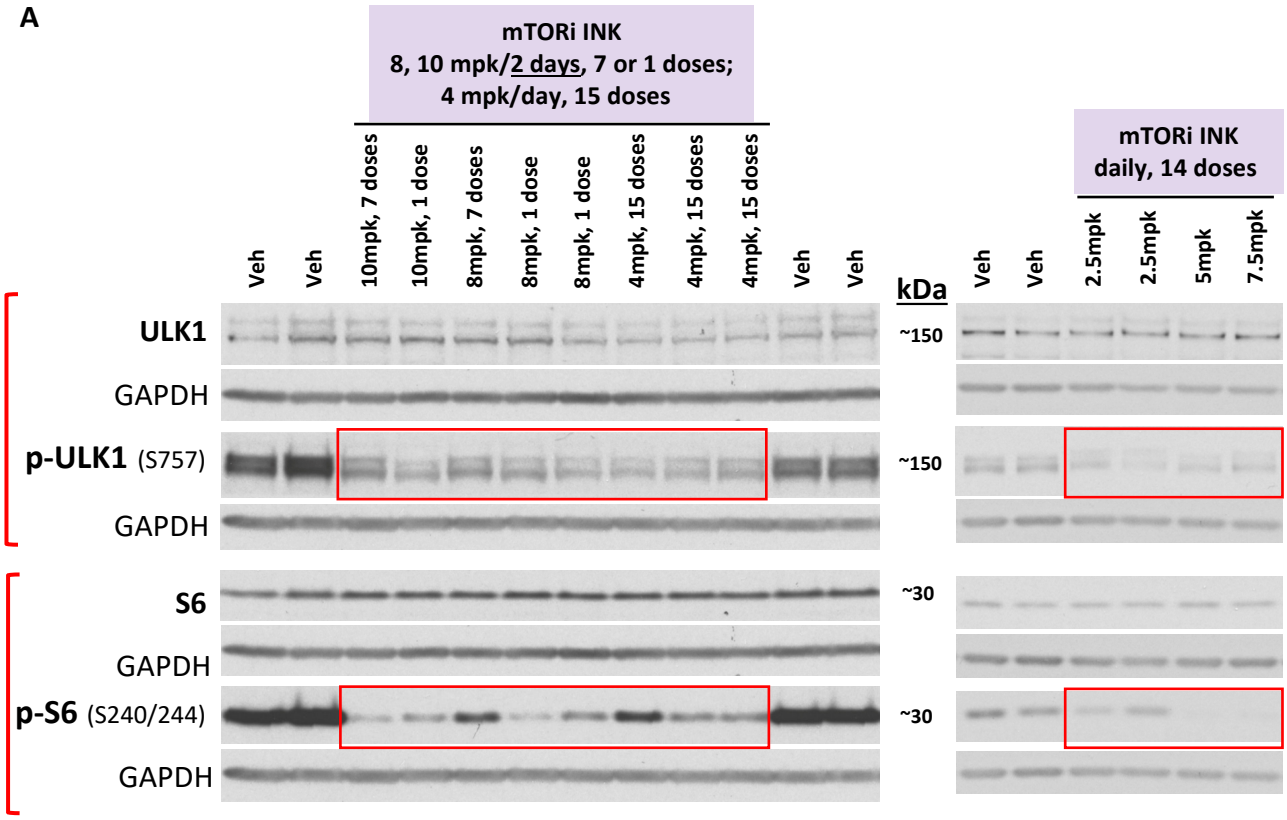
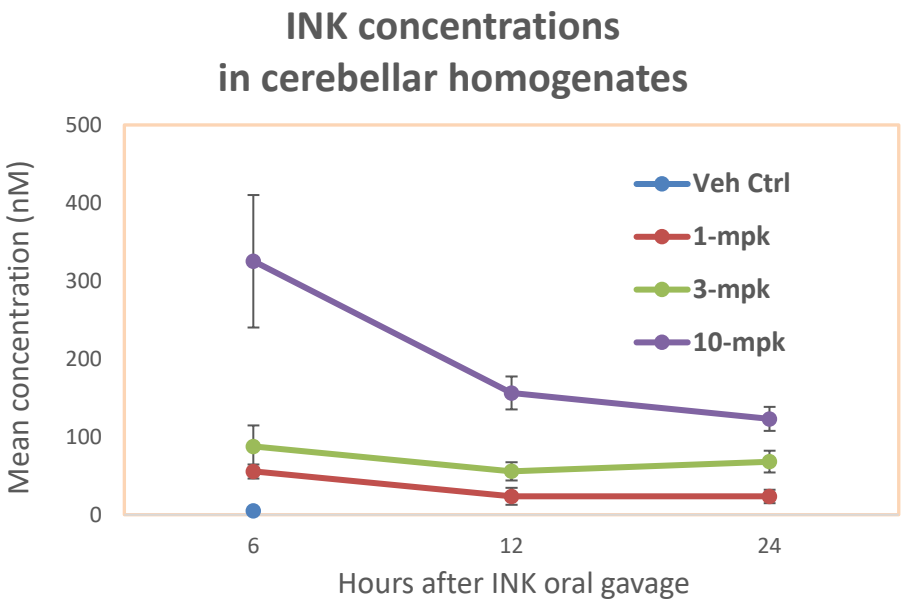
B